
Gas migration pathways and slope failures in the Danube Fan, Black Sea

Hillman Jess I. T. ^{1,5,*}, Klaucke Ingo ¹, Bialas Joerg ¹, Feldman Howard ², Drexler Tina ²,
Awwiller David ², Atgin Orhan ³, Cifci Gunay ³, Badhani Shray ^{4,*}

¹ GEOMAR Helmholtz Ctr Ocean Res, Wischhofstr 1-3, D-24148 Kiel, Germany.

² ExxonMobil Upstream Res, 22777 Springwoods Village Pkwy, Spring, TX 77389 USA.

³ Dokuz Eylul Univ, Inst Marine Sci & Technol, Haydar Aliyev Blvd 100, TR-35340 Izmir, Turkey.

⁴ Ctr Bretagne ZI Pointe Diable, Lab Aleas Geol & Dynam Sedimentaire, CS 10070, F-29280 Plouzane, France.

⁵ GNS Sci, 1 Fairway Dr, Avalon 5010, New Zealand.

* Corresponding authors : Jess I. T. Hillman, email address : j.hillman@gns.cri.nz ; Shray Badhani, email address : Shray.Badhani@ifremer.fr

Abstract :

A large geophysical dataset, including bathymetry, and 2D and 3D P-cable seismic data, revealed evidence of numerous gas flares near the S2 Canyon in the Danube Fan, northwestern Black Sea. This dataset allows us to investigate potential relationships between gas migration pathways, gas vents observed at the seafloor and submarine slope failures. Vertical gas migration structures as revealed in the seismics appear to be concentrated near submarine slope failure structures. Where these seismically defined features extend upwards to the seafloor, they correlate with the location of gas flares. However, not all these structures reach the seafloor, in some cases because they are capped by overlying sediments. A strong correlation is inferred between gas migration pathways, heterogeneous mass transport deposits and contacts between adjacent units of contrasting lithology. Although missing age constrains prevent a final judgement, we discuss the potential relationship between submarine slope failures and gas migration in order to determine if gas migration is a precursor to failure, or if the presence of slope failures and associated mass transport deposits facilitates the migration of gas. Our observations indicate that lithological heterogeneity, mass transport deposits and minor sediment deformation control gas migration pathways and the formation of gas chimney-like features. Gas migration is focused and gradual, resulting in gas flares where the chimney-like features extend to the seafloor, with no evidence of erosive features such as pockmarks.

Highlights

► Identify 3 groups of gas migration structures in seismic data from the Danube Fan. ► Migration structures related to shallow gas migration and flares at the seafloor. ► Gas migration is controlled by lithological heterogeneity and sediment deformation. ► Mass transport deposits play a role in controlling vertical migration occurrence.

Keywords : Gas migration, Chimneys, Gas hydrate, Danube Fan, Slope failure, Black Sea

30 **Introduction**

31 The Black Sea is thought to contain 96×10^9 kg of methane dissolved in the water, with an estimated 1–
32 5×10^{12} m³ of gas hydrates, resulting in a basin-wide flux of methane into the water column of 3.60–
33 4.28 Tg yr^{-1} (Kessler et al., 2006; Starostenko et al., 2010). Reeburgh et al. (1991) and Kessler et al. (2006)
34 concluded that the Black Sea is the largest surface water reservoir of dissolved methane, emitting 0.066
35 Tg yr^{-1} to the atmosphere, with methane concentrations of $>15 \mu\text{M}$ measured in water depths of >100
36 m (Pape et al., 2008). Approximately 68% of the Black Sea basin is thought to be suitable for gas hydrate
37 formation, but evidence of hydrates in the form of bottom simulating reflections (BSRs) within the
38 expected gas hydrate stability zone (GHSZ) has been observed in only a few areas in water depths of
39 600–1800 m (Lüdmann et al., 2004; Popescu et al., 2007; Popescu, 2006; Starostenko et al., 2010;
40 Vasilev and Dimitrov, 2002; Zander et al., 2017b). The best and most widespread BSRs in the Black Sea
41 have been imaged in the Danube Fan area (Popescu et al., 2007, 2006; Zander et al., 2017b). Outlines
42 of the BSR distribution in the Danube Fan by Popescu et al. (2007, 2006) and Zander et al. (2017b) vary
43 slightly depending on the referred data set, but are clearly separated by the Viteaz Canyon. Gas hydrates
44 have been recovered in the Danube Delta (Riboulot et al., 2018), offshore Crimea (Bohrmann et al.,
45 2003; Römer et al., 2012), and offshore Georgia (Heeschen et al., 2011) but without clear evidence of a
46 BSR. These sites are associated with gas emissions (gas flares) at the seafloor (Greinert et al., 2006;
47 Klauke et al., 2006; Römer et al., 2012), but most gas flares in the Black Sea occur in water depths of
48 less than 725 m, i.e. above the GHSZ (Naudts et al., 2006).

49 The precise mechanisms by which gas migrates from depth to reach the seafloor in the Danube Fan are
50 still poorly understood. Understanding shallow gas migration and the potential relationship with the
51 hydrate system in this region is of interest for offshore hydrocarbon exploration due to the potential
52 hazard of shallow gas accumulations when drilling, and also the possible connection to submarine slope
53 failures which pose a risk to seafloor infrastructure. In this study we present seismic data acquired
54 during the R/V Maria S. Merian (MSM34) cruise of 2013–2014 (Figs. 1 and 2) to demonstrate that there

55 are several settings that are conducive to gas migration in the region, including lithological contacts
56 acting as flow pathways and vertical gas migration structures, or gas chimneys. Gas chimneys are
57 defined as an area of low-concentration gas migrating upwards from a gas accumulation at depth
58 (Cartwright, 2007; Gay et al., 2006; Karstens and Berndt, 2015; Koch et al., 2015). Gas chimneys act as
59 conduits for vertical migration of fluid and/or gas and can be imaged in seismic data as anomalies
60 characterized by distorted reflections and low velocities caused by incoherent scattering, absorption
61 and poor stacking due to nonhyperbolic normal moveout (NMO) (Karstens and Berndt, 2015; Løseth et
62 al., 2009; Sheriff, 2011).

63 There are several factors that may play a role in controlling the migration of gas through the sediments.
64 The formation of gas chimneys and other vertical fluid flow anomalies is generally controlled by
65 overpressure-induced hydrofracturing of overlying, low-permeability sediments (Judd and Hovland,
66 2007; Karstens and Berndt, 2015; Mountjoy et al., 2014). Other factors, such as faulting and
67 deformation, lateral gas migration, formation-wide overpressure, and lithological heterogeneity may
68 also play a role (Cartwright et al., 2007; Chenrai and Huuse, 2017; Karstens and Berndt, 2015; Nicoll,
69 2016; Seebeck et al., 2015). Determining how these factors interact may help us in understanding the
70 formation history and location of gas chimneys and flares. In addition, we propose that gas accumulation
71 due to overpressure build up may be one of the driving forces behind the development of gas flares at
72 the seafloor. Lastly, we investigate the potential link between gas migration and slope failure events in
73 the vicinity of a submarine canyon in the Danube Fan.

74 *Geological setting of the Danube Fan*

75 The Danube Fan is a fine-grained turbidite system located in the northwest Black Sea, offshore Romania
76 (Fig. 1 and 2) and consists of a series of stacked channel-levee sequences that have built up over the
77 last ~900 ka (Popescu et al., 2001; Winguth et al., 2000; Wong et al., 1997, 1994; Zander et al., 2017b).
78 The continental shelf here is up to 120 km in width, and the Danube Fan lies downslope of the shelf
79 break (at ~100 m water depth) extending down to the basin floor at depths of >2200 m (Wong et al.,
80 1997). The channel-levee systems of the Danube Fan are characterized by erosional processes in the

81 upper reaches, transitioning to depositional processes in the middle to lower slope (Feldman et al.,
82 2017; Popescu et al., 2001). The Viteaz Canyon was the most recently active canyon in the fan during
83 the last glacial maximum when it was connected directly to the Danube River (Popescu et al. 2001). The
84 development of the submarine canyons that still have a bathymetric expression was initiated ~22 ka,
85 with several smaller canyons being incised prior to the formation of the main Viteaz Canyon (Winguth,
86 1998; Winguth et al., 2000). One such canyon is the S2 Canyon, which lies to the northeast of the Viteaz
87 Canyon and is the focus of this study (Figs. 1 and 2). These features are classified as canyons in the upper
88 reaches where they are incising the shelf edge and dominated by erosional processes, and channels in
89 the outer reaches of the fan where they are dominated by depositional, aggregational processes
90 (Popescu et al., 2001). For consistency, in this study we refer to the two features being discussed as the
91 Viteaz Canyon and the S2 Canyon, as we are primarily concerned with the upper reaches where the
92 canyons incise the shelf edge. The morphology of the canyons and channels in the Danube Fan is
93 influenced by the Coriolis force—a common observation in mid- to high-latitude systems with a right
94 deviation of flow direction in currents in the northern hemisphere (Menard, 1955)—resulting in larger
95 levees on the western side of the canyons (right-hand to the downslope flows) relative to those to the
96 east (Popescu et al., 2001; Zander et al., 2017b). The fan was abandoned as sea level rose at about 7,500
97 years bp, resulting in sediment supply being restricted to nearshore lagoons (Chepalyga, 1984; Lericolais
98 et al., 2013; Martin and Yanko-Hombach, 2011; Panin and Popescu, 2007).

99 A key stratigraphic horizon in the region is the Base Neoeuxinian Sequence Boundary (BNSB), which
100 marks the onset of activity in the Danube Fan during the last sea-level lowstand in the Black Sea (Fig. 3)
101 (Popescu et al., 2001). The BNSB horizon has been dated at ~22 ka using ¹⁴C dating of a sample recovered
102 in core MD04-2762 during the ASSEMBLAGE 1 cruise in 2004 (Lericolais et al., 2013). This sample was
103 recovered ~150 km southeast of the MSM34 study area, and as such, only provides a minimum age for
104 the BNSB. Whilst the MD04-2762 core provides a minimum age for the BNSB, the maximum age of this
105 horizon ~75 ka can be determined using sea level curves as sea level rise prior to 75 ka prevented
106 sedimentation in the Danube Fan (Chepalyga, 1984; Panin and Popescu, 2007).

107 There are four key sedimentary facies in the Danube Fan: mass transport deposits (MTDs), channel fill
108 sediments, lobes and levee deposits (Popescu et al., 2004). Lobes are not significant on the slope and
109 as such are not discussed further here. The other three are characterised in seismic data as follows.

110 1. Mass transport deposits (MTDs), or slumps associated with slope failure events are
111 characterised by hummocky, chaotic and irregular seismic facies, with discontinuous, low to
112 high amplitude reflections (Popescu et al., 2004; Winguth et al., 2000; Zander et al., 2017a).
113 These deposits are interpreted as predominantly fine-grained sediment, with occasional coarse-
114 grained sections in some areas. Although there is some discussion in literature regarding the
115 definition of slope failure related deposits, for the purposes of this study, all deposits associated
116 with slope failure events are referred to as MTDs (Mulder and Alexander, 2001; Mulder and
117 Cochonat, 1996).

118 2. Canyon fill sediments are associated with turbidity-current deposits within the canyons. While
119 canyons are, by definition, erosive, they become partially infilled by such late-stage deposits
120 because of waning turbidity current activity. These are characterised by subparallel, irregular or
121 hummocky reflections along narrow belts with high amplitudes in seismic data (Flood et al.,
122 1991; Konerding, 2008; Lericolais et al., 2013; Winguth et al., 2000). These sediments are
123 predominantly coarse-grained clastics with a high proportion of sand inferred from the seismic
124 response and similar analogs, such as the Amazon Fan (Flood et al., 1991).

125 3. Levee deposits are extensive across the Danube Fan, with the Viteaz Levee sediments extending
126 across much of the study area. Levees are predominantly composed of finely-laminated, fine-
127 grained spill-over turbidites. They may also contain occasional thin, sand-rich intervals that can
128 act as permeable pathways. These are characterised in the seismic data by parallel to
129 convergent, laterally continuous reflections of low to medium amplitudes with an overall
130 wedge-shaped geometry (Popescu et al., 2001; Winguth et al., 2000; Wong et al., 1997).

131 Gas flares in the water column have been recorded in over 5000 locations in the Black Sea and range
132 from seeps related to deep seated mud volcanoes (Greinert et al., 2006) to widespread seepage in water

133 depths shallower than the upper limit of the gas hydrate stability zone (Egorov et al., 2011, 2003; Naudts
134 et al., 2006; Römer et al., 2012; Starostenko et al., 2010). Few gas flares have been observed from within
135 the gas hydrate stability zone (Klaucke et al., 2006; Römer et al., 2012). Upward migration of gas through
136 the sedimentary column is typically associated with structural or lithological contacts, which facilitate
137 the movement of gas and can be imaged in seismic data as so-called gas chimneys, (Bello et al., 2017;
138 Heggland, 2005). It has been suggested that flares in the Black Sea may be aligned along faults, as such
139 structural features commonly act as conduits for fluid and/or gas flow (Popescu et al., 2007). In many
140 cases, there appears to be a direct correlation, based on seismic observations, between the distribution
141 of faults and the occurrence of flares (Popescu et al., 2007). However, they are also observed in the
142 absence of fault systems, frequently in the vicinity of submarine slope failures and canyons (Kutas et al.,
143 2004; Starostenko et al., 2010), or they can be aligned along the crest of submarine ridges (Naudts et
144 al., 2006). Previous studies show that the Viteaz Canyon is located above the presumed offshore
145 position of the Peceneaga-Camena fault; a feature which could act as a migration pathway for gas
146 (Popescu et al., 2004; Winguth et al., 2000).

147 Gas venting in the Black Sea and other areas is commonly observed in conjunction with other seafloor
148 features such as mud volcanoes, pockmarks, bacterial mats and the precipitation of authigenic
149 carbonates (Bohrmann et al., 2003; Gay et al., 2007; Judd and Hovland, 2007; Kessler et al., 2006; Suess,
150 2014). Authigenic carbonates have been observed in the northwest Black Sea in the vicinity of seep sites
151 in water depths of 230–1738 m (Mazzini et al., 2004; Peckmann et al., 2001; Starostenko et al., 2010).
152 The origin of gas in this region is not well constrained, and previous studies have shown evidence of
153 both thermogenic and biogenic sources in the Black Sea region (Olaru-Florea et al., 2014; Starostenko
154 et al., 2010). Data from gas seeps and sediment cores in the northwest region show that the composition
155 of the gas in this area is >99% methane (Popescu et al., 2006; Zander et al., 2017b).

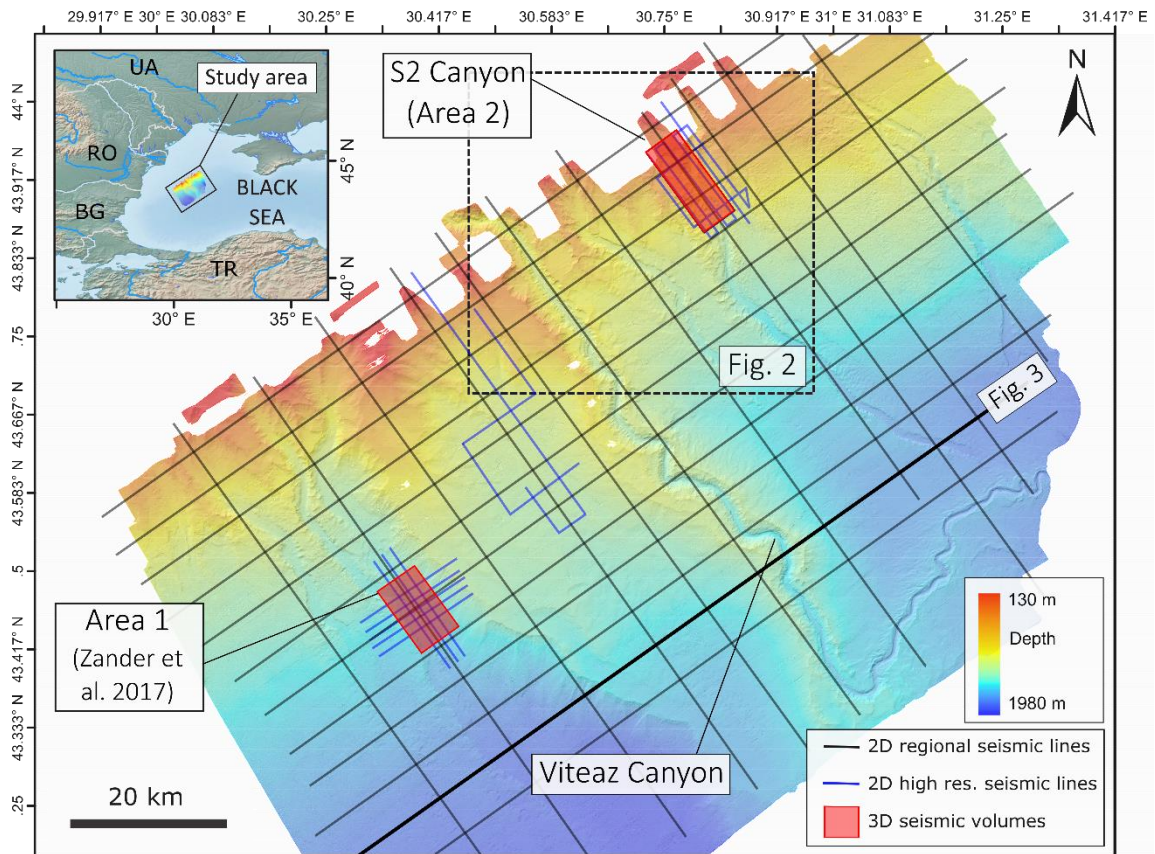


Figure 1 Map of the Danube Fan study area showing the location of the full dataset acquired during the MSM34 cruise. The focus of this paper is the S2 Canyon region in Area 2 (see Fig. 2). Inset: Location of the study area in the northwestern Black Sea. RO = Romania, TR = Turkey, BG = Bulgaria, UA = Ukraine.

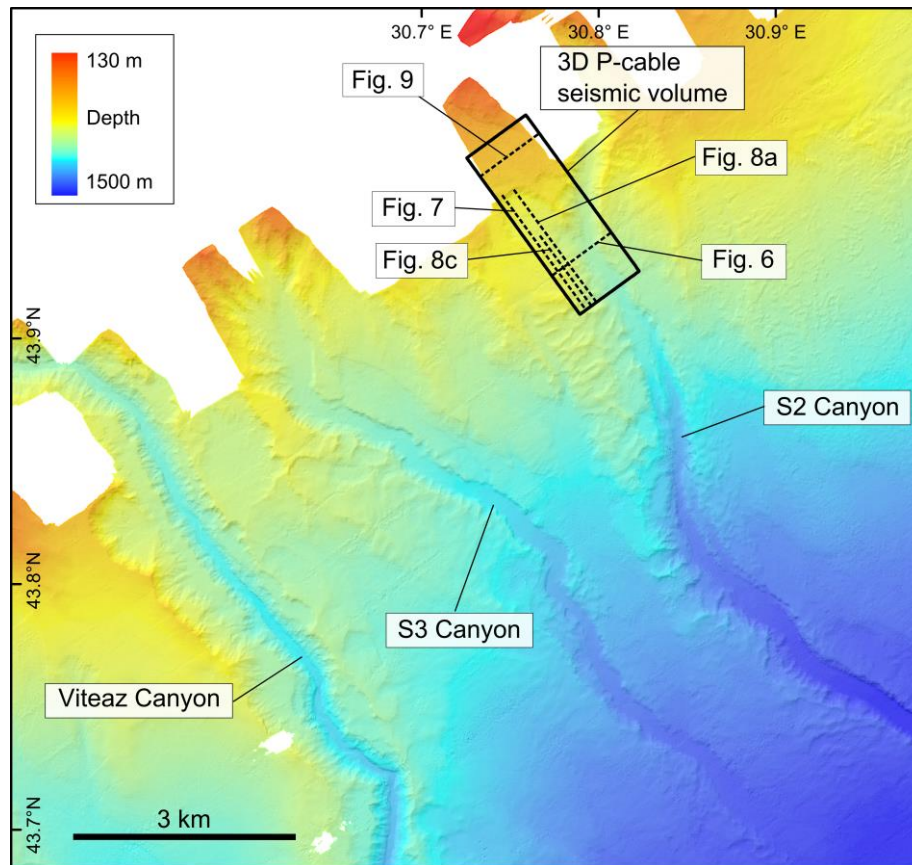


Figure 2 Map of the Danube Fan study area. The location of seismic lines included in this paper is indicated by the black dashed lines.

156 **Gas migration pathways**

157 Evidence of gas migration through the sedimentary column can be observed in seismic data in the form
 158 of enhanced amplitude seismic reflections associated with the presence of free gas in the sediments
 159 (Bünz and Mienert, 2004; Ecker et al., 2000; Hornbach et al., 2003; Max and Johnson, 2014). Free gas in
 160 sediments scatters acoustic energy, resulting in the disturbance of seismic reflections, an effect known
 161 as acoustic turbidity (Judd and Hovland, 2007; Popescu et al., 2007). Where gas content is high, turbidity
 162 may fade out to complete ‘blinking’ where sediments appear to be acoustically impenetrable (Popescu
 163 et al., 2007; Yun et al., 2005). Such features are commonly associated with anomalously high-amplitude
 164 enhanced reflections or bright spots, which result from high concentrations of free gas trapped in the
 165 sediments (Andreassen et al., 2007; Gorman et al., 2002; Karstens and Berndt, 2015). Such
 166 accumulations of free gas result in increased impedance contrast with inverted reflectivity across
 167 horizons due to the anomalously low velocity, and low impedance, of gas bearing sediments (Popescu

168 et al., 2007). Gas chimneys are common in the Black Sea. On the inner shelf these features tend to
169 terminate against a major unconformity which is interpreted as Oligocene to Upper Miocene in age
170 (Gillet et al., 2003; Popescu et al., 2007). On the outer shelf these chimneys may reach the seafloor,
171 resulting in active venting and gas flare formation at the seafloor (Popescu et al., 2007). This is thought
172 to be a function of the permeability of the base of the Miocene sediments, and may also be related to
173 increased localized gas supply as some chimneys are associated with known hydrocarbon fields
174 (Popescu et al., 2007).

175 In addition to supplying gas to flares, gas migration in the subsurface is thought to have played a role in
176 the formation of submarine slope failures (McIver, 1982). Such failures are also found along the shelf
177 break in the Danube Fan (Ker and Riboulot, 2015). Gas hydrates have frequently been linked to
178 submarine slope failures, and it has been proposed that dissociation of hydrates following a shift in the
179 GHSZ due to sea level lowering or seafloor warming may be a factor in slope failure events through
180 generating overpressure and causing sediment destabilisation (Crutchley et al., 2007; Dondurur et al.,
181 2013; Horozal et al., 2017; Li et al., 2016; Mountjoy et al., 2014; Sun et al., 2017). In addition, there is
182 some debate regarding the impact that the presence of gas hydrates has on the stability of sediments.
183 Some studies propose that the presence of gas hydrates in sediments may reduce the stability of slopes
184 as a result of enhanced creep behaviour and high strain-dependence, as demonstrated in laboratory
185 experiments of hydrate-bearing sediments (Handwerger et al., 2017; Mountjoy et al., 2014). Others
186 propose that hydrates act as a cement, strengthening the sediment and thereby reducing slope failure
187 occurrence (Winters et al., 2007; Yoneda et al., 2016). A recent paper by Elger et al. (2018) suggests
188 that overpressure at the base of hydrate stability results in the formation of pipes, which transfer
189 overpressure to shallow depth and contribute to destabilization of a slope.

190 **Data and methods**

191 During the MSM34 cruise, multibeam bathymetry data, sub-bottom profiler data, regional 2D seismic
192 lines, high resolution 2D lines, and high resolution 3D P-cable seismic volume were acquired (Figs. 1 and
193 2) (Bialas et al., 2014). A grid of regional 2D multichannel seismic profiles was acquired as

194 reconnaissance data across the entire Danube Fan. A high-resolution set of 2D multichannel seismic
 195 lines and a 3D multichannel seismic cube were acquired across a slope failure structure next to the S2
 196 Canyon, hereafter referred to as the S2 slump. Multibeam bathymetry data were acquired using a 12
 197 kHz, hull mounted Simrad® EM122 multibeam echosounder. Bathymetry data were processed onboard
 198 using MB-systems® and gridded at a resolution of 25 m x 25 m. Sub-bottom profiler data were acquired
 199 using an Atlas Parasound PS70 hull mounted parametric echosounder system. The system operated
 200 with primary frequencies of 18 and 22 kHz resulting in 4.0 kHz secondary (parametric) signal and a beam
 201 width of 4.5–5.0°. The parametric frequency was used to image shallow subsurface structures and
 202 stratigraphy, with a maximum penetration of 200 ms TWT. During the second leg of the cruise (MSM34-
 203 2) the lower primary frequency (18 kHz) was used for water column imaging to detect gas flares.

204 *Seismic data acquisition*

205 The acquisition parameters for the three seismic data types acquired during the MSM34 cruise are
 206 summarised in Table 1.

207 **Table 1** Summary of acquisition parameters for seismic surveys included in this study (Fig. 1). Nominal
 208 vessel speed of 3.5 knots.

	2D regional lines	2D high resolution lines	3D P-cable volume
Source	45 in ³ / 45 in ³ GI gun, shot interval 18.75 m, source depth 2 m	45 in ³ / 45 in ³ GI gun, shot interval of 3 s, source depth 2 m	45 in ³ / 45 in ³ GI gun, shot interval of 3 s, source depth 2 m
Streamer	HydroScience SeaMUX Digital-bidirectional, 1050 m long, 168 channels, 6.25 m group interval, 8 hydrophones per group. Record length 45 s max. Streamer depth 4 m.	225 m long, 144 channel streamer. Vibration isolation section of 25 m, 55 m tow cable and 19 active sections of 12.5 m length. Total active length of 237.5 m.	Streamer depth 2 m. 20 streamers towed in parallel, active sections of 12.5 m length, 8 channels per section.
Data acquired	2114 km	110 km	30 km ²

209 *2D seismic data processing*

210 Processing of the regional 2D seismic data consisted of correction of the navigation data, signal-
 211 processing, stacking, semblance picking and true-amplitude time migration. No gain was applied during

212 processing. The regional seismic lines have a CDP spacing of 3.12 m and a centre frequency of 70 Hz.
213 The high resolution seismic lines have a CDP spacing of 1.5625 m, with a centre frequency of 130 Hz
214 (Bialas et al., 2014; Zander et al., 2017b). The streamers used for the high resolution seismic lines are
215 too short for semblance analysis. The velocity information for the regional seismic profiles was therefore
216 extrapolated to the high-resolution data. Both data types were converted from time to depth domain
217 using the velocity information derived from the regional seismic lines and cross-checked with P-wave
218 velocities from ocean bottom seismometers that were available in the study area (Bialas et al., 2014;
219 Zander et al., 2017b).

220 *P-cable 3D seismic data processing*

221 Processing of the 3D seismic data included shot and receiver repositioning, shot based signal processing,
222 a low-cut frequency filter of 28 Hz, a 3D marine cable filter (3D FK-dip-filt) and lastly, trace balancing.
223 The data was then binned to a grid of 3.125 x 3.125 m and stacked with a fairly averaged NMO, followed
224 by a post-stack trace interpolation. Post stack time-migration was conducted using an extended 3D Stolt
225 migration followed by a 2-pass frequency domain (residual) migration inline-crossline. This was done
226 using a simple velocity model with a water velocity of 1482 m/s. The 3D volume was then depth
227 converted using a pseudo-3D depth variant velocity model constructed using ocean bottom
228 seismometer (OBS) data acquired during the MSM34 cruise.

229 *Seismic and sequence stratigraphic interpretation*

230 Both the 2D and 3D seismic data were loaded into IHS Kingdom® for the interpretation of key horizons
231 and structures. The 2D seismic data acquired during MSM34 were used to map out regional stratigraphic
232 horizons across the Danube submarine fan complex to provide relative age constraints for the
233 development of the S2 channel–levee complex, and the S2 slump. Interpretation of the BNSB surface
234 was based on the location of the sequence boundary as per Popescu et al. (2001) and modified based
235 on the new seismic data available in this study and at ExxonMobil Upstream Research Company
236 (EMURC).

237 **Results**

238 The key stratigraphic horizons and units identified in the seismics are summarized in Table 2 and Figs. 3
 239 and 4. In addition to the key lithological and stratigraphic units, a distinct BSR was identified in the 2D
 240 and 3D seismic data across the Danube Fan. In some areas of the fan the BSR is characterized as a clear
 241 reflection that is phase-reversed relative to the seafloor, roughly mimics seafloor topography and cross-
 242 cuts strata. However, in the vicinity of the S2 Canyon in the 3D seismic volume the BSR is characterized
 243 instead by the abrupt termination of high amplitude reflections at a depth of 90-120 m below the
 244 seafloor, creating a distinct boundary, with clear phase reversal of cross-cutting reflections (Fig. 5).

245 **Table 2** Summary of key units (Fig. 3) and geomorphological features (Fig. 4) identified in the MSM34
 246 seismic data.

Unit	Seismic Characteristics	Extent / Location
Viteaz Levee	Parallel to convergent, laterally continuous reflections with low to medium amplitudes. Wedge shaped geometry with increased thickness on the western flank of the Viteaz Canyon. Interpreted as slit/clay rich sediment associated with turbidity currents. Higher amplitude reflections interpreted as coarse-grained, sand-rich horizons.	Located along flanks of the main Viteaz Canyon at the center of the Danube Fan (Figs. 2 and 3). Extends across the full lateral extent of the seismic dataset, thinning with distance from the canyon.
S2 Levee	Parallel to convergent, laterally continuous reflections with low amplitudes. Wedge shaped unit that is generally thicker to the west of the S2 Canyon. Interpreted as slit/clay rich sediment associated with turbidity currents.	Located along the flanks of the S2 Canyon. Narrow extent laterally, constrained to ~7 km west and ~4 km east of the S2 Canyon.
MTD 1		Located directly above the BNSB. Extends across ~3200 km ² of the Danube Fan with maximum thickness between the S2 and Viteaz Canyons (Fig. 3).
MTD 2	Irregular, chaotic, discontinuous reflections with variable amplitudes. Interpreted as predominantly fine-grained material with some coarse-grained sediment, highly heterogeneous across units.	Located between the S2 and Viteaz Canyons, with maximum thickness immediately west of the latter (Fig. 3). Extends across ~520 km ² of the fan.
MTD 3 (see Fig. 9)		Located at the seafloor, forming the 'floor' of Slump A. Average thickness of the unit is 25 m. The unit is not fully mapped in the MSM34 seismic data.

MTD 4 (see Fig. 5)	Chaotic, discontinuous reflections with variable seismic amplitude beneath the S2 Slump scar. Interpreted as predominantly fine-grained material with some coarse-grained sediment, highly heterogeneous across units.	Located beneath S2 Slump, discontinuous when mapped out across the 3D seismic data. Base of the deposits is not consistently imaged in the seismic data due to limited signal penetration.
-----------------------	--	--

Feature	Characteristics	Extent / Location
Slump A	Elongate downslope feature that extends ~6 km upslope of the S2 slump headwall. Headwall of the slump is slightly crenulated and has been incised by younger canyon features (Ker and Riboulot, 2015). Average height of the headwall is 10 m, average width is 2.6 km.	Upslope of the S2 Slump (Figs. 2 and 4), covers ~20 km ² , not fully mapped in MSM34 data – extent estimated from Ker and Riboulot (2015).
Slump B	Small slump adjacent to the S2 Canyon with a relatively smooth headwall.	Southwest flank of the S2 Canyon in water depths of 540 to 650 m (Figs. 2 and 4), covers ~3 km ² .
S2 Slump	Well defined, horseshoe shaped feature with a relatively smooth headwall. Average height of the headwall is 55 m, average width is 2.2 km.	Southwest flank of the S2 Canyon in water depths of 560 to 790 m, downslope of Slump A and Slump B (Figs. 2 and 4), covers ~8 km ² .

247 Sequence Stratigraphy

248 Based on stratigraphic interpretation of more extensive datasets available at EMURC, the BNSB has been
 249 identified in the MSM34 dataset as the prominent regional unconformity at the base of the widespread
 250 MTD 1 (Fig. 3). Above the BNSB, several other stratigraphic horizons were mapped across the extent of
 251 the 2D seismic data, delineating 4 key stratigraphic units (Fig. 3). These are MTD 1, the levee associated
 252 with the S2 Canyon, MTD 2, and the extensive levee associated with main Danube/Viteaz Canyon (Fig.
 253 3).

254 Based on the interpreted sequence stratigraphy and the absolute age estimates presented above,
 255 sedimentation rates can be calculated for the key sediment packages in the Danube Fan and these are
 256 summarised in Table 3.

257 **Table 3** Sedimentation rates for the Danube Fan, calculated using average unit thickness along Line 11
 258 (see Fig. 3). **In the absence of core samples to establish the precise nature of the formation MTD 1, we*
 259 *assign a nominal duration of 1 ka for the purpose of the calculation.*

Unit	Age (ka BP)	Duration (ka)	Average thickness (m)	Volume (km ³)	Sedimentation rate (m/ka)
------	----------------	------------------	--------------------------	------------------------------	------------------------------

Viteaz Levee	19-7.5	11.5	170.53	1161.86	14.8
S2 Levee	21-19	2	47.35	5.50	23.68
MTD 1	22-21	<1*	239.19	596.32	239.19

260 Gas flares

261 During the MSM34 cruise several acoustic anomalies in the water column were imaged in the high
 262 frequency sub-bottom profiler data (Fig. 5). Most of these occur at approximate water depths of
 263 ~665 m, which correlates to the calculated top of the GHSZ. Several of the flares were observed during
 264 multiple crossings. Gas flares are abundant near the S2 Canyon and S2 slump, with several gas flares
 265 imaged along the headwall and sidewalls of the S2 slump (Figs. 4 and 5).

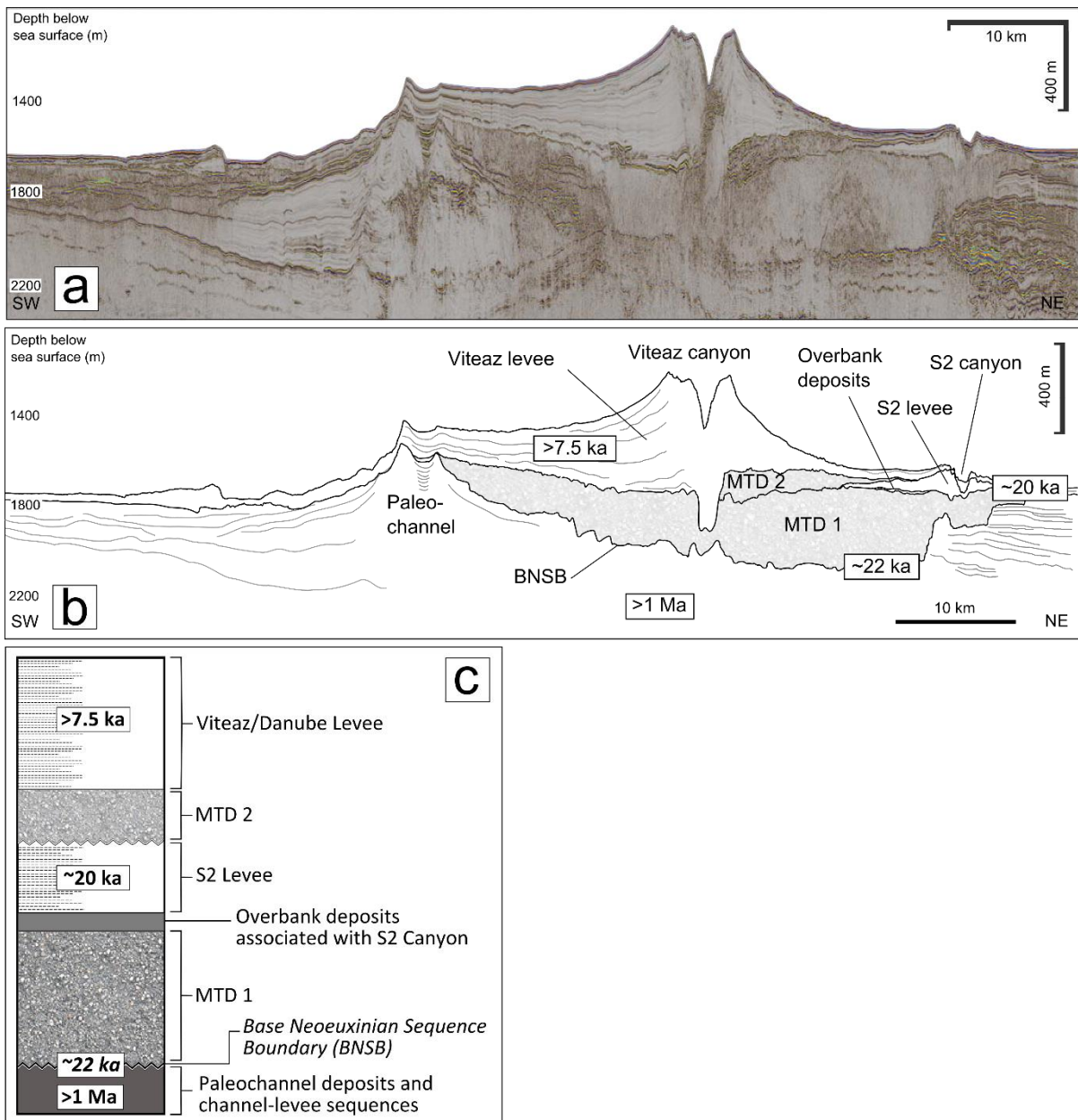


Figure 3 a) Seismic Line 11. b) Line drawing of the interpreted seismic line (Line 11). BNSB = base Neoeuxinian sequence boundary, MTD = mass transport deposit. For location of the seismic line see Fig. 1. c) Schematic stratigraphic column of the key units in the Danube Fan that are the focus of this study.

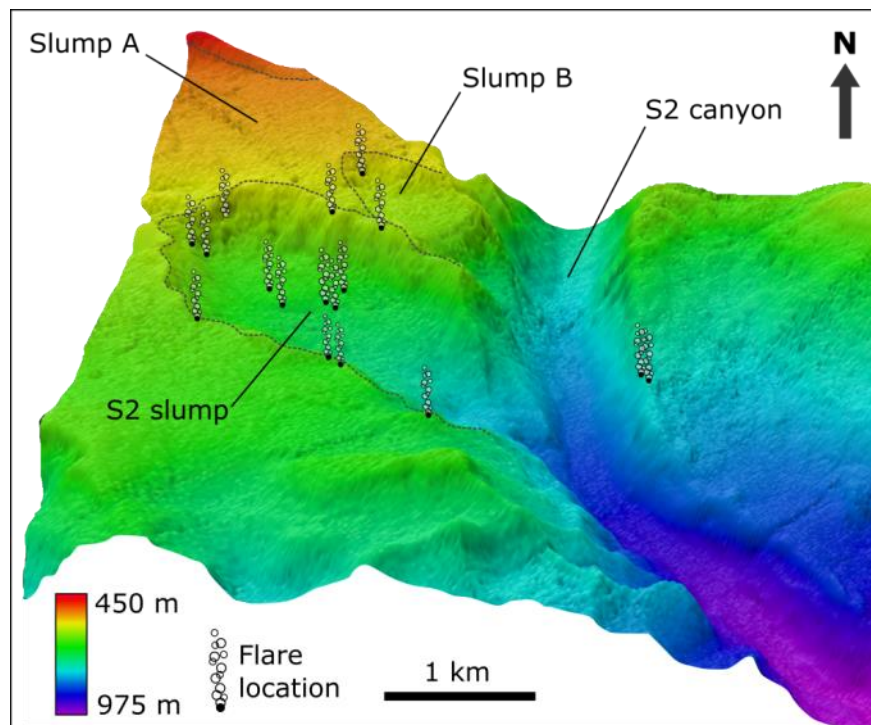


Figure 4 3D perspective view of the S2 canyon and slump to show the location of flares identified during the MSM34 cruise in the area. The dashed lines delineate the edges of the 3 slope failure features – the S2 slump, slump A, and slump B. The majority of slump A is not imaged in the MSM34 bathymetry; however, this can be identified clearly in the bathymetric data acquired during the GHASS cruise (Ker and Riboulot, 2015). For the purposes of the 3D visualization, a 10x vertical exaggeration has been applied.

266 Gas migration pathways

267 The seismic data acquired during cruise MSM34 show several amplitude anomalies that are interpreted
 268 as potential gas migration pathways. They are subdivided into migration pathways related to lithology,
 269 and gas chimney-like structures.

270 Migration pathways related to lithology

271 In the vicinity of the S2 slump the BSR is closer to the seafloor than in adjacent areas, although the BSR
 272 does not actually intersect the seafloor in the seismic data (Figs. 6 and 7). In this area, the BSR appears
 273 to approach the base of the chaotic, deformed strata (MTD 4) beneath the S2 slump (Fig. 7). Beneath
 274 the S2 Canyon, the BSR is clearly defined by the termination of several high amplitude reflections, with
 275 patches of enhanced amplitudes along the BSR and in the sediments underlying the S2 slump. Several

276 of these high amplitude reflection packages near the seafloor underlie the southwestern sidewall of the
 277 S2 slump (Fig. 8), and correlate with the position of observed flares at the seafloor.

278 In the levee sediments to the northeast of the S2 Canyon, there are two high amplitude horizons; at the
 279 base of the package of well-laminated near seafloor sediments, and within a unit characterized by
 280 relatively seismically transparent facies (Fig. 6). These two horizons are truncated along the canyon wall
 281 and correlate with the position of flares observed during the MSM34 cruise. A similar relationship is
 282 observed further to the northeast along the canyon.

283 *Gas migration structures*

284 In the seismic data, numerous structures have been identified that are tens-of-meters in diameter,
 285 conical in geometry, and are capped by high amplitudes underlain by zones of acoustic blanking (Figs.
 286 7–10). Based on observations in the seismic data these structures can be categorized into Groups A, B
 287 and C, based on their dimensions, amplitude characteristics and geometry (Table 3).

288 **Table 3** Characteristics of the 3 groups of vertical migration structures identified in the MSM34 seismic
 289 data.

	Group A	Group B	Group C
Number	26	15	7
Geometry	Narrow (10s to 100s of m), steep sided structures	Conical, narrow peak (10s to 100s m) and broad base (several 100 m)	Varied, some broad and elongate, others patchy and dispersed
Amplitude characteristics	High amplitude at top, with blanking or dimmed amplitudes below	High amplitude at the peak and to the edges, with blanking or dimmed amplitudes at the center of the structure	Broad area of high amplitudes, or patchy, dispersed high amplitudes, less well defined
Active migration?	Associated with active flares where they extend to the seafloor	Associated with active flares where they extend to the seafloor	Associated with active flares where they extend to the seafloor

290 The structures in Group A and B are both characterized by distinct high amplitude anomalies, and/or
 291 acoustic blanking, and are differentiated primarily by their geometry and size, with Group B being more
 292 complex in structure and larger in size (100s of m in diameter). Group B are also frequently associated
 293 with high amplitude strata at depth, which fade into zones of acoustic blanking at the base of these

294 structures (e.g. Fig. 8). Several of the larger features in Group B show stacked concentric circles of high
295 seismic amplitudes, centered on a zone of acoustic blanking (Fig. 9). Both Group A and B are
296 characterized by distinct chimney-like shapes, with circular to elliptical horizontal geometry when
297 observed in the 3D seismic data. Group C are less well defined in the seismic data, and do not exhibit
298 the same 'chimney-like' shape, with some characterized by discrete, broad high-amplitude anomalies,
299 and others as clusters of chaotic seismic facies with patchy high amplitudes (e.g. Fig. 8).

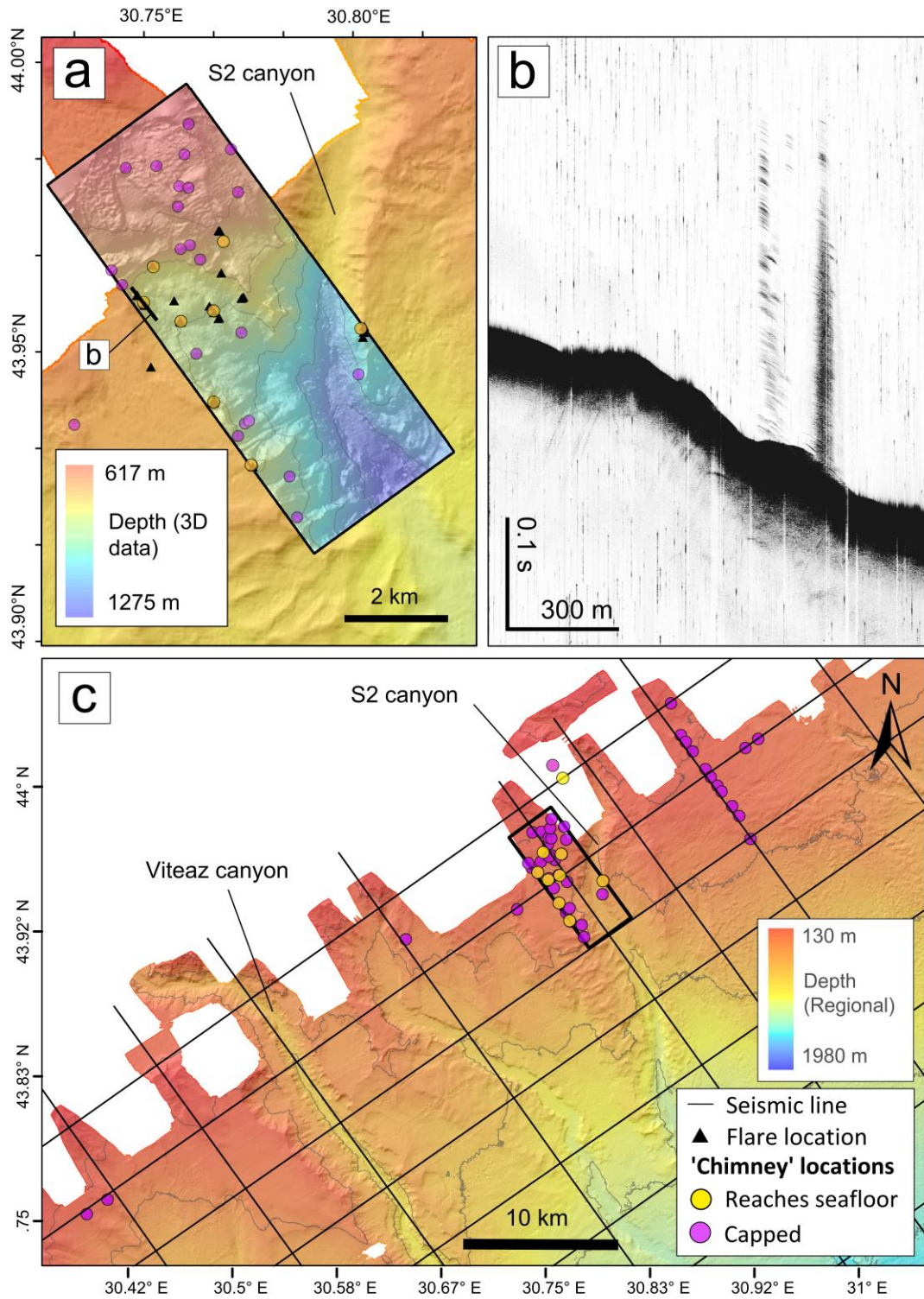


Figure 5 a) Map of gas migration structures identified in seismic data, and flares observed in high frequency sub-bottom profiler data in the vicinity of the S2 canyon. b) Example of a flare observed in the water column, location of the line is shown in (a). c) Map of gas migration structures identified in seismic data across the MSM34 study area.

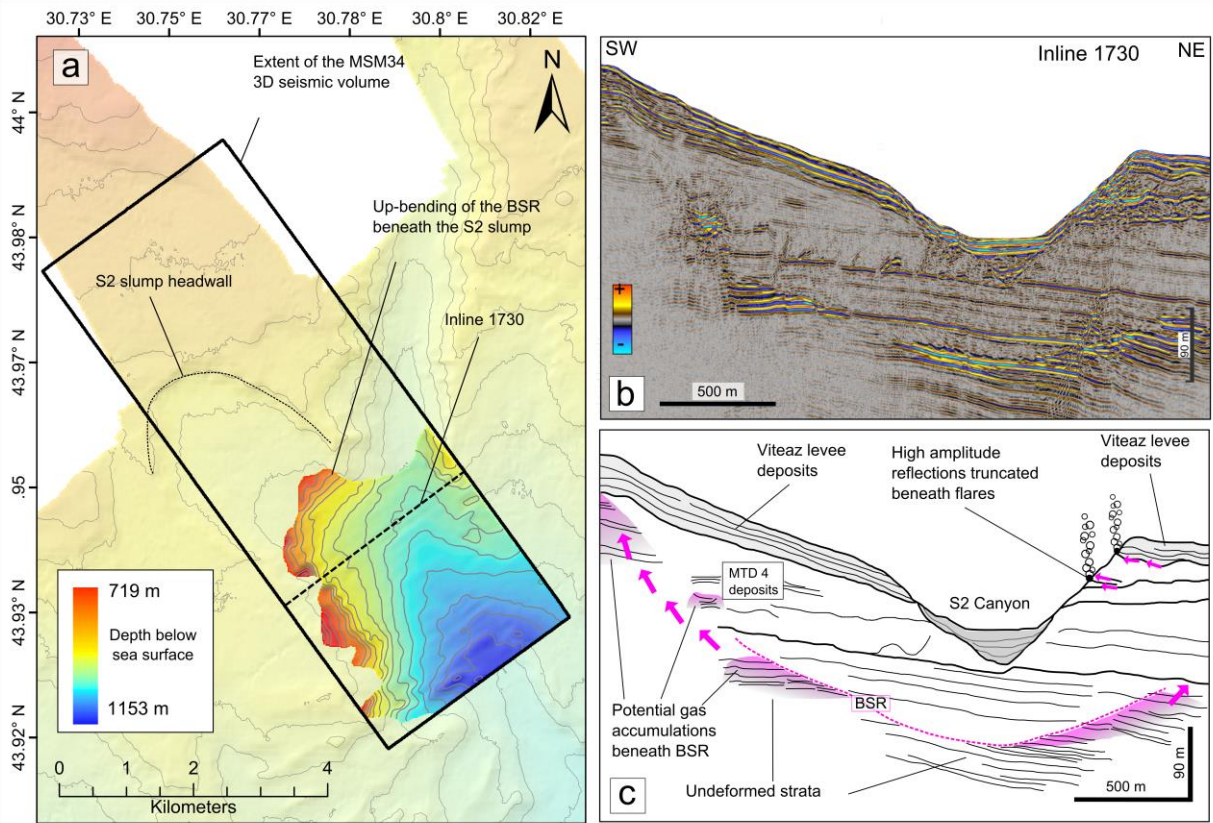


Figure 6 a) Map to show the extent of the BSR in the 3D seismic data. The S2 slump headwall is outlined on the seafloor bathymetry for reference. b) Inline 1730: seismic profile. c) Inline 1730: Line drawing. The BSR bends upward beneath the S2 slump. Increased amplitudes terminating and stacking along the potential pathway of the BSR image vertical gas migration leading to potential gas accumulations near the seafloor along the southwestern sidewall of the S2 slump. Along its eastern flank the S2 Canyon truncates two high-amplitude horizons in the levee deposits that correlate to the position of flares along the canyon.

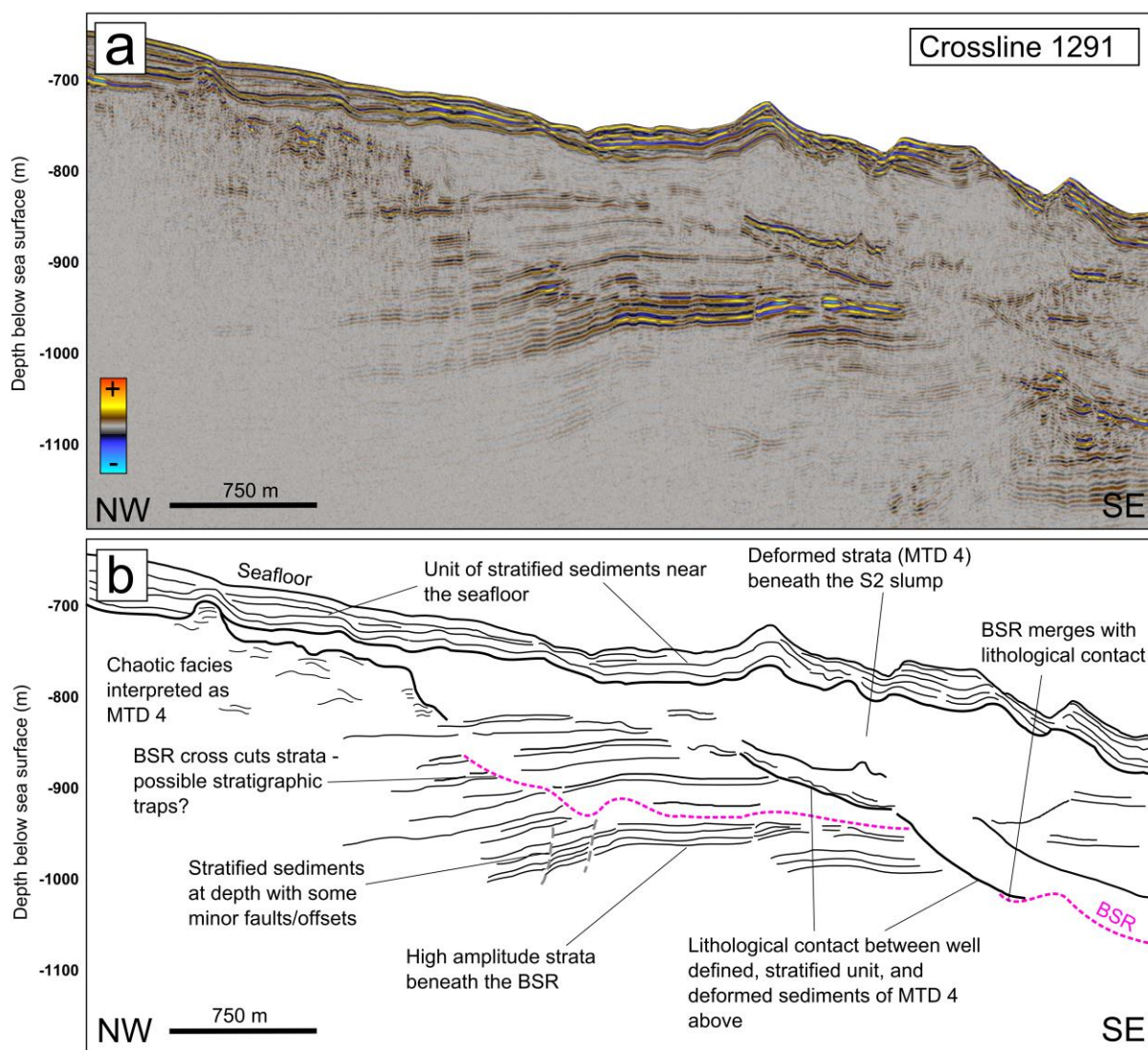


Figure 7 a) Crossline 1291: seismic line showing the position of the BSR relative the lithological contact beneath the MTD. The position of the BSR is reinforced through observations of Inline 1730 (Fig. 6). See Fig. 2 for line location. b) Crossline 1291: interpreted line drawing. The position of the BSR merges with the lithological contact to the SE. To the NW the BSR is clearly distinguished by the termination of high amplitudes. The stratified sediments beneath the BSR are offset by minor faults, with possible small stratigraphic traps along the BSR.

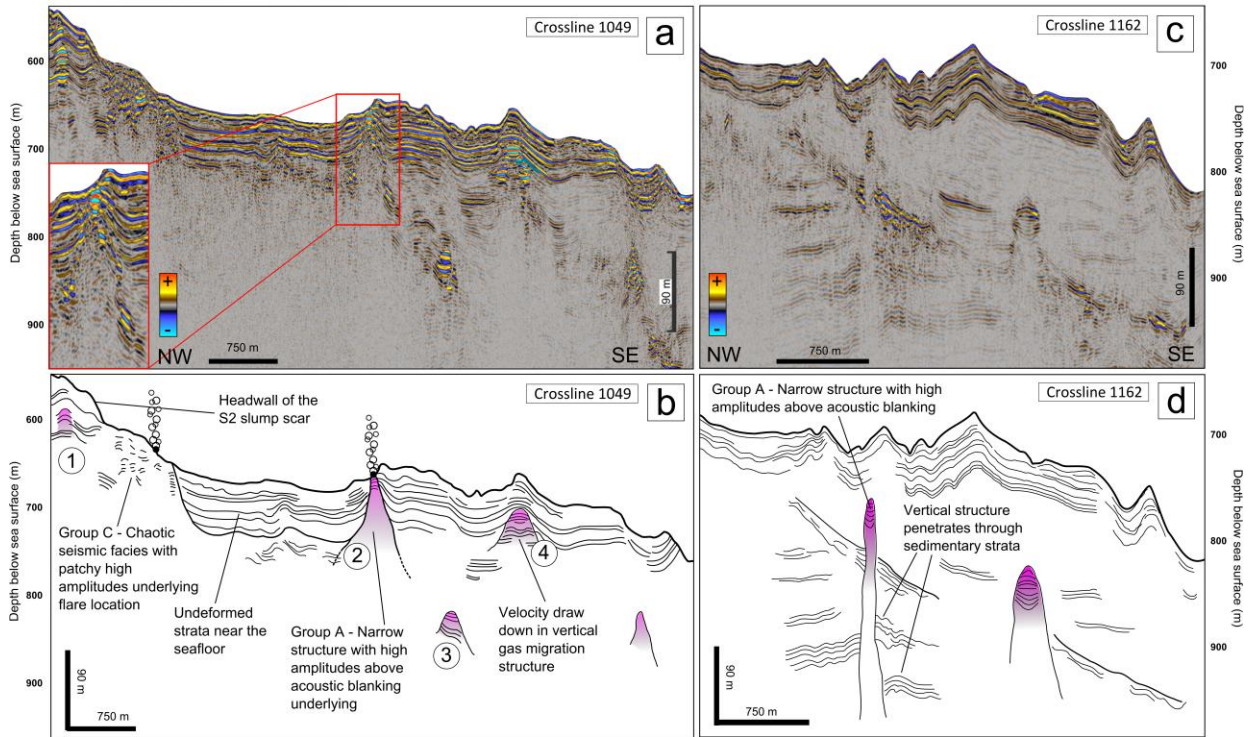


Figure 8 a) Crossline 1049: seismic line showing examples of Group A and C gas migration features. Inset – enlarged view of narrow, conical structure showing high amplitude reflections capping a column of acoustic blanking. See Fig. 2 for line location. b) Crossline 1049: interpreted line drawing. Structures 1, 3 and 4 are capped by overlying sediments and do not reach the seafloor. Structure 2 reaches the seafloor and underlies the location of an identified flare. There is also a flare above the chaotic seismic facies interpreted as MTD deposits associated with the S2 slump. c) Crossline 1162: seismic line showing an example of Group A gas migration features. See Fig. 2 for line location. d) Crossline 1162: interpreted line drawing. These narrow, vertical structures clearly cross-cut the sedimentary strata at depth.

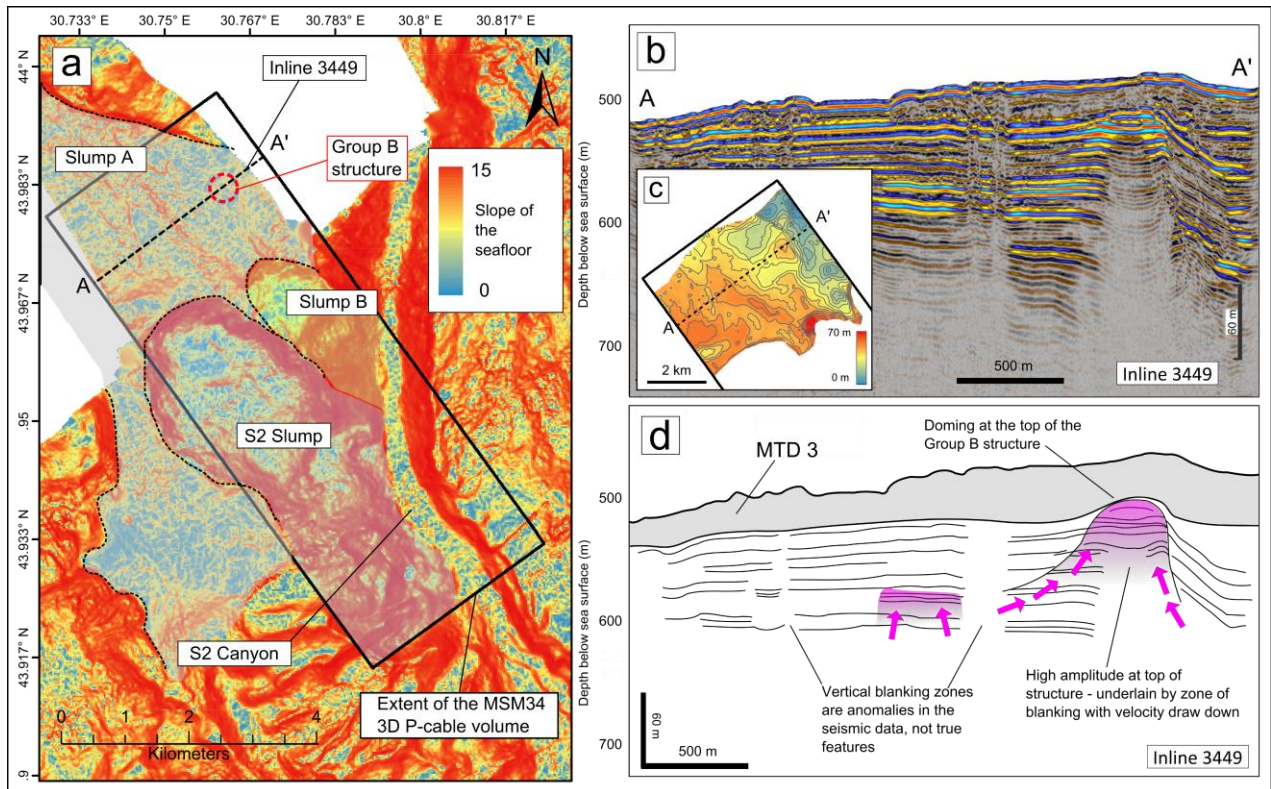


Figure 9 a) Slope map of the seafloor – the three slump features near the S2 canyon are outlined. Slump A is associated with MTD 3, shown in (b) and (d) that caps the chimney. b) Line 3449: seismic line showing an example of a Group B gas migration structure. c) Isopach map of the MTD 3 unit. The thickness of the unit decreases above the large gas-migration feature and dome structure (c) in the NE of the study area. The heavy black line indicates the extent of the 3D seismic volume. d) Line 3449: interpreted line drawing. The Group B structure here does not reach the seafloor; it is capped by MTD 3 associated with the slope failure (Slump A) upslope of the S2 slump. There appears to be doming at the top of the structure, resulting in thinning of the overlying sediments.

300 Discussion

301 Sequence stratigraphy

302 Our interpretation of the regional seismic stratigraphy differs from previous work such as Popescu et al.
 303 (2001), who interpret the BNSB as a shallower horizon underlying a smaller MTD 2 (see Fig. 3). The major
 304 change between the older interpretations of the position of the BNSB and ours presented in this paper,
 305 is that Popescu et al. (2001) placed the sequence boundary above the S2 levee (Popescu et al 2001,
 306 their Fig. 3), and we are placing it well below the S2 levee. However; there is general consensus that the
 307 sequence boundary is below a major MTD that occurs just at the base of the Late Pleistocene fan (For
 308 example Popescu et al. 2001 Fig. 4; Constantinescu et al. 2015 Fig. 3). The new seismic data allows the
 309 relationship between the MTD that rests on the sequence boundary (MTD 1) and the S2 levee to be

310 established without ambiguity, and the MTD seen in the Popescu et al. (2001) and Constantinescu et al.
311 (2015) figures is well below the S2 levee confirming that the S2 levee is within the Late Pleistocene fan.
312 Since the S2 levee is below the main levee of the Late Pleistocene fan, it represents a channel system
313 that was active briefly after MTD 1 was deposited (~22 ka), and before the main channel was occupied.
314 As our sedimentation rate estimates are based on widely spaced regional 2D seismic lines, there is some
315 uncertainty in the calculations (Table 3); however, the calculated values provide an indication of the
316 relative sedimentation rates in the region. Due to the difference in our sequence stratigraphic
317 interpretations to those of previous studies, these values are significantly higher than those of Winguth
318 et al. (2000).

319 *Nature of the observed seismic anomalies*

320 We interpret the high amplitude horizons (Fig. 6) as gas-charged sediments that are supplying gas to
321 the flares where they are truncated by the S2 Canyon. In several locations, particularly within the large
322 levee deposits of the Viteaz Canyon, there are discrete patches of high seismic amplitudes along some
323 strata. This could be the result of lateral migration of gas along these strata, forming shallow
324 accumulations of gas within the levee sediments. The vertical, sub circular to elliptical disruptive
325 features, on the other hand, are most likely associated with gas migration, with Group A and B
326 comprising more classical chimney structures, and Group C as anomalous features associated with gas
327 migration and/or accumulation. While these structures may not exhibit all the characteristics of 'true'
328 seismic chimneys, they are certainly indicative of upward gas migration through sediments that has
329 resulted in the formation of vertical features characterized by regions of acoustic blanking and capped
330 by high amplitudes that may be interpreted as gas accumulations. 48 such structures are observed in
331 the MSM34 seismic data, with the majority clustered in the vicinity of the S2 Canyon; however, there is
332 an inherent data bias here due to the location of the 3D seismic volume. Those that do reach the seafloor
333 correlate to the position of flares observed during the cruise, indicating that there is active upward
334 migration of gas occurring. However, there are also vertical gas migration structures that accumulate

335 gas at their summit, being 'capped' by the overlying sediments and do not extend to the seafloor (Figs.
336 5 and 8).

337 These gas migration structures appear to be restricted to water depths of <700 m, with none identified
338 in the seismic data in the more distal reaches of the Danube Fan. Some of the structures in Group B that
339 do not reach the seafloor (i.e. those that are capped by overlying sediment), show evidence of doming
340 above the chimneys, with reduced thickness in the overlying sediment package (Fig. 9). The structure in
341 Fig. 9 seems to appear in connection with a local summit of the base MTD C horizon. Based on the
342 interpretation of these horizons across the extent of the 3D seismic volume, this local summit is likely
343 an effect of doming caused by gas, which results in upward bending of the strata. Horizontal layering of
344 the neighbouring sediments would not be expected in case of tectonically forced folding.

345 *Formation and role of gas chimneys in gas migration*

346 There are several factors that may control the upward propagation of gas and the formation of these
347 chimney-like structures; the rate of gas supply, contrasting lithology forming seals and localized
348 variations in lithological properties such as porosity and permeability. Here we discuss the factors that
349 likely influenced the formation of the three groups of structures identified in the MSM34 seismic data.

350 *Group A structures*

351 The structures in Group A are characterized as narrow, steep sided gas migration features, with an
352 overall simple geometry, somewhat similar to those observed offshore Norway (Karstens and Berndt,
353 2015), Namibia (Moss and Cartwright, 2010), northern Australia (Rollet et al., 2009), and in the Congo
354 Basin (Gay et al., 2006; Ho et al., 2012). Several such structures are observed beneath the S2 slump,
355 where they appear to correlate with locations where the overlying unit of stratified sediments thins out
356 (Fig. 8), suggesting that upward gas migration exploits the thinned, weakened overburden at such
357 points. The high seismic amplitudes observed at the peak of these structures are indicative of shallow
358 gas accumulations (Rollet et al., 2009). However, as some of these chimney-like structures are capped
359 and do not extend to the seafloor, the gas accumulation most likely did not result into an overpressure

360 strong enough to initiate fracturing (Cathles et al., 2010; Karstens and Berndt, 2015). Where these
361 chimney-like structures do reach the seafloor, they correlate to the observed flares. The absence of any
362 resolvable erosional features, or pockmarks, at the seafloor above these features again suggests that
363 the venting is gradual and focused (Moss and Cartwright, 2010), compared to the intermittent more
364 explosive, blow-out type venting observed in locations such as offshore Nigeria (Løseth et al., 2011).
365 Pockmarks are, however, observed upslope of the study area in water depths of ~500 m, and further to
366 the northwest along the shelf edge (Riboulot et al., 2017).

367 *Group B structures*

368 The structures in Group B are generally larger in size, typically with a more complex internal geometry
369 than those of Group A. In particular, the near-circular, capped gas migration structures upslope of the
370 S2 slump (Fig. 9) have a geometry that is reminiscent of a larger (km-scale) feature observed in 2D
371 seismic data on the Hikurangi Margin, offshore New Zealand. There, high amplitudes that correlate with
372 high seismic velocities (~2150 m/s) are observed on the edges of a chimney-like feature, with blanking
373 and low velocities (~1850 m/s) at the center and below (~1600 m/s) (Fraser et al., 2016). This is
374 interpreted as gas hydrates forming at the boundary of the chimney structure (corresponding to high
375 seismic amplitudes and velocities), with free gas at the center (corresponding to seismic blanking and
376 low velocities). A similar interpretation could be possible here; however, given that these structures lie
377 above the predicted GHSZ, it is more likely that the high seismic amplitudes correspond to free gas
378 accumulations at the edges of the structures, rather than hydrate. The presence of free gas in sediments
379 can be characterized in seismic data by both high and low amplitudes (Ecker et al., 2000; Hornbach et
380 al., 2003), and it may be that the variation across these chimney structures is due to a change in the
381 concentration of free gas in the sediments, or the degree of disruption in the sediments caused by the
382 upward flow of free gas (Cathles et al., 2010; Karstens and Berndt, 2015).

383 In addition to the 'stacked rings' that characterize the chimneys upslope of the S2 slump (Fig. 9), there
384 is also evidence of seafloor doming above some of the capped chimney structures, along with possible
385 deformation of the sediments (Fig. 9). Flattening the seismic volume along a horizon that caps this

386 chimney structure (i.e. the base of MTD 3) reveals decreased sedimentation above the domed chimney,
387 which is consistent with previous work by Koch et al. (2015) on similar structures in the very shallow
388 subsurface offshore New Zealand. The fact that the domed structures are preserved in the subsurface
389 indicates that the dome morphology can sustain burial, as suggested by Koch et al. (2015). This would
390 suggest that the MTD unit capping the gas migration structure was deposited following the
391 development of the gas chimneys in this region. Based on the stratigraphic relationships, Slump A (Fig.
392 4) pre-dates the S2 slump, and therefore this unit must have been deposited prior to ~20 ka, providing
393 a minimum age constraint for the development of the gas chimneys. However; precise timing of the
394 development of individual chimneys is not possible. Gas doming has been observed elsewhere in the
395 Black Sea on the Turkish continental slope (Golmshtok et al., 1992). In that location, the dome reaches
396 the seafloor and correlates with the location of a gas vent at the seafloor. The absence of a high
397 amplitude 'cap' at the apex of the capped chimneys may be related to the deposition of MTD 3 (Fig. 9),
398 as the deposition of this unit may have eroded the top of the original chimney structure (which may
399 have been connected to the seafloor), resulting in a sealed vertical migration pathway. Potentially as a
400 result of limited gas supply, the original high amplitude 'cap' has not been replenished since this
401 occurred. The possible deformation of sediments in the vicinity of these larger chimney structures (e.g.
402 Fig. 9), suggests that this deformation, or minor folding, of the sediments may have resulted in gas being
403 channeled towards a particular location, allowing the buildup of an accumulation sufficient to generate
404 hydrofracturing and form a large chimney.

405 *Group C structures*

406 While the structures in Groups A and B can be interpreted as true gas migration structures, with many
407 of the typical features of chimneys, those in Group C are more anomalous and do not follow the same
408 characteristics. Some of the structures in Group C are likely the result of small, shallow gas
409 accumulations, similar to those described by Andreassen et al. (2007) in the Barents Sea, the locations
410 of which are controlled by minor structural traps in the channel-levee complexes of the Danube Fan..
411 The structures in Group C that are associated with flares at the seafloor are characterized by patchy

412 distributions of high amplitudes in the seismic data (e.g. Figs. 6 and 8). These are likely due to the
413 dispersed accumulation of gas within the sediments, which may be controlled by localized, small-scale
414 heterogeneity in the lithology (Deckers, 2015; Thöle et al., 2016). This is particularly evident at the foot
415 of the S2 slump headwall, where the MTD is exposed at the seafloor, and corresponds with the location
416 of several flares (Figs. 4 and 10).

417 *Evidence of gas beneath the BGHSZ and hydrofracturing*

418 Beneath the BSR gas saturation generally increases with proximity towards the BSR (Berndt et al., 2004).
419 In the vicinity of the S2 Canyon, high amplitude reflections abruptly terminate at the BSR, indicating that
420 gas migration/accumulation is focused along certain stratigraphic intervals, as was also observed in
421 other hydrate provinces (e.g. Vanneste et al., 2001). Beneath the S2 channel, the BSR appears to act as
422 a seal, preventing upward gas migration beneath the canyon. However, to the west, underlying the S2
423 slump, the BSR is warped upward. Increased amplitudes terminate along the BSR appear at irregular
424 intervals and with variable strength (Fig. 6 & 7). The upward continuation of the BSR leads to patches of
425 high amplitudes near the seafloor, some of which correlate to flares in the water column. Vertical
426 correlated stacks of high amplitudes next to the seafloor in correlation with active gas expulsion at the
427 seafloor suggests that gas may be migrating along the BGHS as it bends upward beneath the slump
428 deposits, and that gas is then 'leaking' from beneath the BSR and may be forming accumulations of free
429 gas near the seafloor and forming small gas chimneys that feed the observed flares. This is further
430 evidenced by the observation of several flares along the northern edge of the S2 Canyon (Fig. 6). These
431 flares correlate with the truncation of high amplitude reflections and minor disturbances in the
432 sediments along the edge of the canyon (Figs. 6 and 10), indicating that free gas may be migrating along
433 these horizons, forming flares where they are exposed at the seafloor. Levee deposits consist of fine
434 grained muds, with intermittent beds of silty and sandy sediments, as observed in cores recovered from
435 this region (Constantinescu et al., 2015; Lericolais et al., 2013). We therefore interpret these high
436 amplitude reflections as coarser grained sediments with higher porosity and permeability which

437 facilitate the migration of free gas through the levee towards the canyon whereas fine-grained, muddy
438 units hinder vertical gas migration.

439 *Mass transport deposits and gas migration*

440 It should be noted that within a chaotic body such as an MTD there are other possible explanations for
441 high amplitude patches in the seismic data, such as variations in lithology. Without additional data from
442 core samples, it is not possible to rule this out in this location. It is not immediately apparent as to why
443 some structures are capped, and others extend to the seafloor. Based on the observation of the position
444 of the BSR corresponding with the base of MTD 4 deposits beneath the S2 slump scar in the seismic
445 data, it would appear that the sediments of MTD 4 also facilitate the migration of gas, with
446 discontinuities in the chaotic seismic facies likely providing flow conduits that result in the formation of
447 gas migration features and flares (Thöle et al., 2016). Upward migration of gas through the sediments
448 is also prevented by MTD deposits in some cases (Sun et al., 2017). This would explain the capped
449 structures that are observed upslope of the S2 slump (Figs. 4 and 9). The chimneys terminate at the
450 contact with the MTD 3 associated with Slump A, which indicates that the sediments of the MTD form
451 a seal, preventing upward gas migration. While minor variations in porosity and/or permeability of
452 sediments may already be sufficient to allow or control the movement of gas. This is of particular
453 significance in the case of MTD sediments as these are highly heterogeneous and have limited lateral
454 connectivity (Manley et al., 1997; Moscardelli et al., 2006; Piper et al., 1997). The high concentration of
455 vertical gas migration features within MTD 4 supports this, indicating that the positions at which these
456 structures are able to propagate upwards through the MTD sediments may correlate to sediments with
457 slightly higher porosity/permeability.

458 MTD deposits on continental slopes generally involve a mixture of lithologies from the original failed
459 area and transported by various gravitational processes (Mulder and Cochonat, 1996). Short transport
460 distances would prevent effective sorting and consequently result in low permeability of the MTD,
461 forming a seal unit, unless the failed deposits were already well sorted. As the primary source of failed
462 material in the Danube Fan is likely to be levee sediments presenting a mixture of fine-grained and

463 slightly coarser spill-over deposits. The thickness of deposits from failure of such material most likely
464 corresponds to sealing effectiveness as shown by the correlation between the thickness of the MTD 4
465 and the location of flares, which generally occur where the MTD thins to <25 m. On the other hand,
466 active gas migration structures capped by an MTD unit should lead to gas accumulation at the base of
467 the MTD, or to gas migration along its base. We do observe increased amplitudes at the top of some of
468 these capped structures (Fig. 8), but this could also be the effect of the impedance contrast between
469 the MTD und underlying deposits. It is also possible that gas flow rates have been low since the MTDs
470 were emplaced, resulting in limited accumulation and lateral migration of gas underlying those MTD
471 units that act as seals.

472 Hydrofracturing

473 Geochemical analysis of porewater samples during the MSM34 cruise indicates that a dry gas system is
474 present in the Danube Fan, with little to no gas dissolved in porewater (Bialas et al. 2014, Haeckel, pers.
475 comm. 2016). Amplitude anomalies within the gas chimneys observed in the MSM34 seismic data occur
476 preferentially along the continuation of high amplitude horizons (Fig. 9) (Chenrai and Huuse, 2017; Koch
477 et al., 2015). This could be due to gas gradually accumulating over a period of time at one stratigraphic
478 horizon, until a sufficient volume builds up to exceed the overburden pressure, at this point
479 hydrofracturing occurs, and the gas migrates upward. This would lead to the development of a series of
480 stacked gas accumulations in the sediment column, forming a chimney-like structure, as observed in the
481 seismic data (Fig. 9). In order for hydrofracturing to occur, the pressure must exceed the combined least
482 principle stress and tensile strength of the sediment (Karstens and Berndt, 2015; Maestrelli et al., 2017).
483 The buoyancy of free gas exerts a localized pressure on the seal unit, which is directly proportional to
484 the column height of the gas accumulation (Cathles et al., 2010). The height of the gas column required
485 to breach the overburden seal can be calculated using the following equation (Karstens and Berndt,
486 2015):

$$487 \quad P_{wm} = P_{wn}(\gamma_{wc} / \gamma_{wn})$$

488 where P_{wm} is the capillary pressure between methane and water, P_{wn} is the capillary pressure between
489 nitrogen and water (3 MPa), γ_{wc} is the interfacial tension coefficient for methane and water at 7.5 MPa
490 and 13.94°C (65×10^{-3} N/m; Khosharay and Varaminian, 2013), and γ_{wn} is the interfacial tension
491 coefficient for nitrogen and water (72.8×10^{-3} N/m) (Karstens and Berndt, 2015). As an estimate for the
492 locations of gas accumulation we average the imaged depth to the base of the chimneys imaged in our
493 seismic data, therefore P_{wm} can be calculated as 2.679 MPa, assuming only vertical gas migration. It
494 should be noted that a continuous gas column is one possible end-member of the potential saturation
495 spectrum. This value for P_{wm} can therefore be used to determine the gas column height required to
496 breach the overburden seal, using the following equation (Karstens and Berndt, 2015; Zander et al.,
497 2017b):

$$498 \quad H_{hf} = P_{wm} / (g \times (\rho_w - \rho_{CH_4}))$$

499 where H_{hf} is the gas column height required for hydrofracturing to occur, g is the gravitational
500 acceleration (9.81 m/s^2), ρ_w is the density of formation water (1025 kg/m^3) (Karstens and Berndt, 2015;
501 Zander et al., 2017b), and ρ_{CH_4} is the density of methane (58.54 kg/m^3) (calculated for values of 7.5 MPa
502 and 13.94°C using the SUGAR Toolbox; Kossel et al., 2013). Based on this calculation, the gas column
503 height required for hydrofracturing would be 283 m. The average depth to the base of the chimney
504 structures in our seismic data is 158.3 mbsf, indicating that gas column height alone would be
505 insufficient to result in hydrofracturing and seal breaching. However, due to the limited depth of
506 penetration in our seismic data, we are not able to definitively image the base of the chimneys, and as
507 such, there is a significant margin of error in the calculation.

508 Due to the limited depth of penetration in the seismic data the source of the gas that is feeding into
509 these structures is unclear. However, in the vicinity of the S2 slump the position of the BSR correlates
510 with a lithological contact between an MTD 3nd underlying layered sediments. This suggests that the
511 boundary between the two units may be acting as a migration pathway for gas along the base of gas
512 hydrate stability (BGHS) (Fig. 7). This is consistent with the observation of flares overlying chaotic seismic

513 facies interpreted as MTD higher up the slope in the S2 slump. In this location, the MTD is exposed at
 514 the seafloor and provide a gas conduit to feed the flares (Fig. 8 and 10). Unfortunately, in our seismic
 515 data we are unable to image the base of these structures. Geochemical data suggest that the gas is
 516 biogenic in origin (Bialas et al., 2014). Although deeper thermogenic reservoirs may be present in the
 517 area (Olaru-Florea et al., 2014; Starostenko et al., 2010), there is no evidence to suggest that these are
 518 connected to the near-surface gas system.

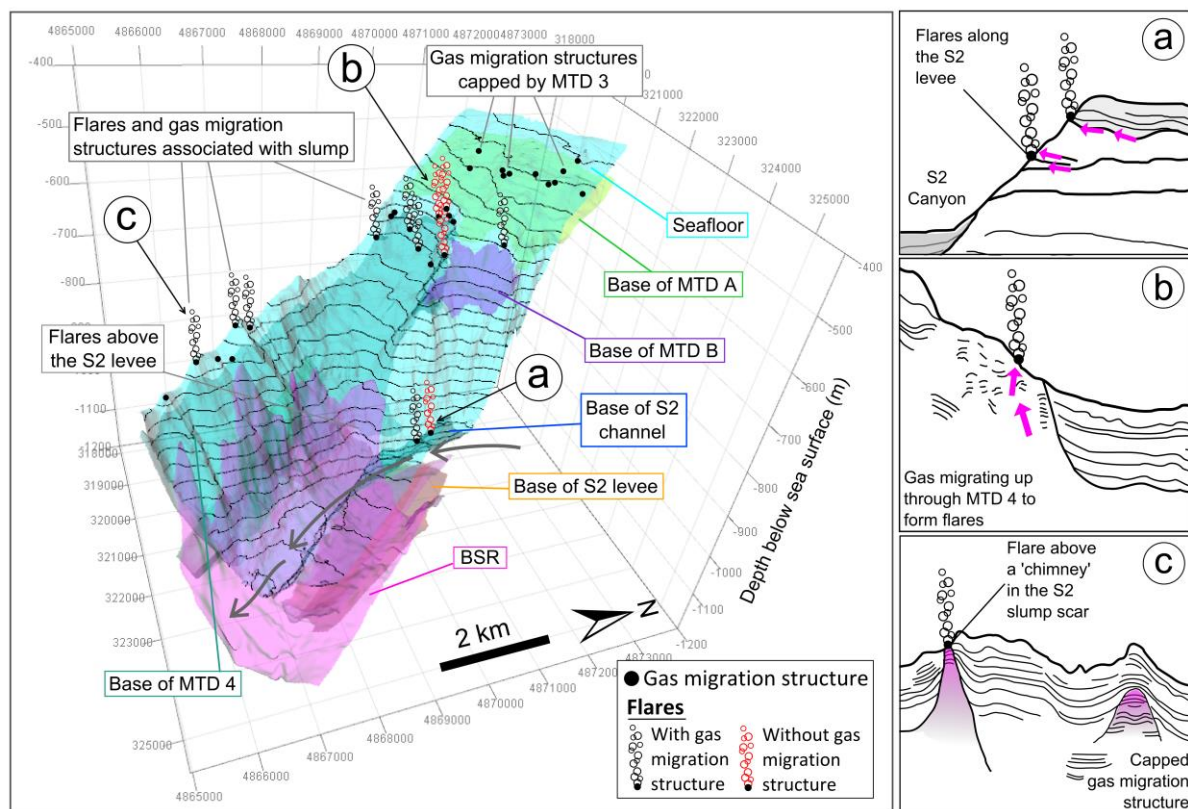


Figure 10 3D view of the BSR, flares and gas migration structures in relation to key stratigraphic units across the extent of the 3D seismic volume. a) Gas charged horizons truncated by the S2 canyon forming flares. b) Chaotic MTD unit allowing upward migration of gas to form flares in the S2 slump. c) Gas migration structure extending upwards to the seafloor along the western edge of the S2 slump, and a capped gas migration structure. In this area gas clearly migrates up from beneath the up-bending BSR (see Fig. 4).

519 Gas migration and submarine slope failure?

520 There are several ways in which gas hydrates may influence slope stability and potentially contribute to
 521 the formation of submarine landslides; overpressure beneath low-permeability, hydrate-bearing
 522 sediments resulting in hydrofracturing, dissociation of hydrates resulting in excess pore pressure, and
 523 plastic deformation of hydrate-bearing sediments causing glacier-style deformation of sediments

524 (Crutchley et al., 2010; Mountjoy et al., 2014; Phrampus and Hornbach, 2012). There is no evidence of
525 the latter style of deformation in this area so this will not be discussed further. Studies in other regions
526 (Li et al., 2016; Mountjoy et al., 2014), have proposed that hydrates may play a role in triggering slope
527 failure due to the build-up of overpressure in high porosity sediments beneath low-permeability,
528 hydrate-bearing sediments in the GHSZ. The removal of large volumes of sediment during such an event
529 could then further destabilise hydrates due to a change in the thermal regime of the near seafloor
530 sediments. However, in the upper section of the sediment column the pressure would likely be
531 hydrostatic and therefore removal of near-seafloor sediments would not necessarily impact hydrate
532 stability in terms of pressure.

533 In the vicinity of the S2 canyon there are three large submarine slope failures (Slump A, B and the S2
534 slump (Fig. 4; Table 2), Slump A is the oldest, and the S2 slump the most recent. The average height of
535 the headwall scarp at the S2 slump is ~25 m, resulting in an estimated volume of 0.36 km³ of sediment
536 being removed in this slope failure event (Badhani, 2016). However, there is no evidence for deposits
537 downslope or in the canyon that could be related to this event suggesting that the S2 Canyon was active
538 at the time of the slope failure.

539 Previous work in the Monterey (Locat and Lee, 2002) and Cook Strait (Mountjoy et al., 2009) canyons
540 indicates that undercutting at the toe of a slope due to the erosive action of hyperpycnal turbidity
541 currents in canyons may result in axial incision of the canyon floor, triggering slope failure due to
542 oversteepening. In case of the S2, oversteepening due to the canyon undercutting likely played a role
543 as well but overpressure generation due to rapid deposition of slope sediments may have also
544 contributed to slope instability.

545 Based on the relative timing of the slope failures surrounding the S2 Canyon, and the observed seafloor
546 doming beneath MTD 3, we can determine that at least some of the gas migration structures have been
547 active since prior to the slope failures occurred. The deposition of the MTD units then capped many of
548 the gas migration structures; however, some have been able to breach this unit and extend to the

549 seafloor to form active gas flares (Fig. 10). Whether the structures reach the seafloor or not appears to
550 be primarily controlled by the thickness and lithology of the overlying sediment, with thinner, chaotic
551 MTD units being readily breached along the slope failure scarp of the S2 slump, resulting in a
552 concentration of flares in this area.

553 **Conclusions**

554 Gas migration structures are abundant in the vicinity of the S2 Canyon and the surrounding sediments
555 of the Danube Fan, occurring at water depths of <700 m. Where these chimneys reach the seafloor,
556 they correspond to observed gas flares in the water column. We classified the structures into three
557 groups based on their seismic characteristics, size, and geometry. Groups A and B are more reminiscent
558 of true gas chimneys at varying scales and complexities, whereas Group C contains anomalous gas
559 accumulations and features related to MTDs. The location of these structures appears to be controlled
560 by: a) overlying units acting as seals, b) variations in lithology across heterogeneous sediments
561 (particularly MTDs), and c) intermittent/gradual gas supply leading to the development of stacked
562 accumulations of gas. The MTD units identified in the 3D seismic volume appear to have contrasting
563 lithological properties; MTD 3 is thicker and acts as a seal, preventing upward gas migration from several
564 structures, whereas MTD 4 is more irregular in thickness, and seems to facilitate the migration of gas
565 through the chaotic seismic facies, resulting in the formation of numerous flares. A clear determination
566 of the source of the gas is not possible, but geochemical data indicate that it is biogenic in origin.

567 Slump events probably resulting from erosive undercutting, but gas migration may have played a role
568 in the initiation of the slope failures. Abundant evidence for gas migration in the area suggests a
569 connection between the slumps and gas migration, although it is not clear whether gas migration
570 facilitates slope failure through overpressure and pre-conditioning of the sediments, or vice versa.
571 However, the capped structures indicate that in others there may be insufficient gas supply to exceed
572 the overburden pressure of the sediments. The younger, chaotic sediments of MTD 4 facilitate the
573 upward migration of gas, particularly around the headwall where the MTD is thinnest, resulting in the
574 concentration of gas flares in this area.

575 **Acknowledgements**

576 This research was funded by ExxonMobil Upstream Research Company. The research cruise MSM34
577 received funding from the European Union Seventh Framework Programme (FP7/2007– 2013) under
578 the MIDAS project, grant agreement No. 603418, from the German Ministry of Education and Research
579 (BMBF) and the Federal Ministry of Economy and Energy (BMWi) through the SUGAR project (Grant
580 Nos. 03G0819A, 03SX320A, 03G0856A). The regional multi-channel seismic data was kindly provided by
581 the Institute of Marine Science and Technology (IMST-Seislab) of the Dokuz-Eylül University, Izmir,
582 Turkey. We would like to thank the captains and crew of RV MARIA S. MERIAN cruise MSM34 as well as
583 the GEOMAR lab technicians for their excellent support. We especially thank Dirk Klaeschen, Anke
584 Dannowski and Cord Papenberg for their help with seismic and OBS data processing.

585 **References**

- 586 Andreassen, K., Nilssen, E.G., Ødegaard, C.M., 2007. Analysis of shallow gas and fluid migration within
587 the Plio-Pleistocene sedimentary succession of the SW Barents Sea continental margin using 3D
588 seismic data. *Geo-Marine Lett.* 27, 155–171. <https://doi.org/10.1007/s00367-007-0071-5>
- 589 Badhani, S., 2016. Slope failures and gas hydrate distribution in the Danube deep-sea fan, NW Black Sea.
590 MSc. Thesis. Christian Albrechts University of Kiel.
- 591 Bello, A., Heggland, R., Peacock, D.C.P., 2017. Pressure significance of gas chimneys. *Mar. Pet. Geol.* 86,
592 402–407. <https://doi.org/10.1016/j.marpetgeo.2017.06.005>
- 593 Berndt, C., Bünz, S., Clayton, T., Mienert, J., Saunders, M., 2004. Seismic character of bottom simulating
594 reflectors: examples from the mid-Norwegian margin. *Mar. Pet. Geol.* 21, 723–733.
595 <https://doi.org/10.1016/j.marpetgeo.2004.02.003>
- 596 Bialas, J., Klaucke, I., Haeckel, M., 2014. MSM-34 / 1 & 2 SUGAR Site Cruise Report. Kiel, Germany.
- 597 Bohrmann, G., Ivanov, M., Foucher, J.-P., Spiess, V., Bialas, J., Greinert, J., Weinrebe, W., Abegg, F., Aloisi,
598 G., Artemov, Y., Blinova, V., Drews, M., Heidersdorf, F., Krabbenhoft, A., Klaucke, I., Krastel, S.,
599 Leder, T., Polikarpov, I., Saburova, M., Schmale, O., Seifert, R., Volkonskaya, A., Zillmer, M., 2003.
600 Mud volcanoes and gas hydrates in the Black Sea: new data from Dvurechenskii and Odessa mud
601 volcanoes. *Geo-Marine Lett.* 23, 239–249. <https://doi.org/10.1007/s00367-003-0157-7>
- 602 Bünz, S., Mienert, J., 2004. Acoustic imaging of gas hydrate and free gas at the Storegga Slide. *J. Geophys.*
603 *Res. Solid Earth* 109, 1–15. <https://doi.org/10.1029/2003JB002863>
- 604 Cartwright, J., 2007. The impact of 3D seismic data on the understanding of compaction, fluid flow and
605 diagenesis in sedimentary basins. *J. Geol. Soc. London.* 164, 881–893.
606 <https://doi.org/10.1144/0016-76492006-143>
- 607 Cartwright, J., Huuse, M., Aplin, A., 2007. Seal bypass systems. *Am. Assoc. Pet. Geol. Bull.* 91, 1141–
608 1166. <https://doi.org/10.1306/04090705181>

- 609 Cathles, L.M., Su, Z., Chen, D., 2010. The physics of gas chimney and pockmark formation, with
610 implications for assessment of seafloor hazards and gas sequestration. *Mar. Pet. Geol.* 27, 82–91.
611 <https://doi.org/10.1016/j.marpetgeo.2009.09.010>
- 612 Chenrai, P., Huuse, M., 2017. Pockmark formation by porewater expulsion during rapid progradation in
613 the offshore Taranaki Basin, New Zealand. *Mar. Pet. Geol.* 82, 399–413.
614 <https://doi.org/10.1016/j.marpetgeo.2017.02.017>
- 615 Chepalyga, A.L., 1984. Inland sea basins, in: Velichko, A.A., Wright, H.E., Barnowsky, C.W. (Eds.), *Late*
616 *Quaternary Environments of the Soviet Union*. University of Minnesota Press, Minneapolis, pp.
617 229–247.
- 618 Constantinescu, A.M., Toucanne, S., Dennielou, B., Jorry, S.J., Mulder, T., Lericolais, G., 2015. Evolution
619 of the danube deep-sea fan since the last glacial maximum: New insights into Black Sea water-level
620 fluctuations. *Mar. Geol.* 367, 50–68. <https://doi.org/10.1016/j.margeo.2015.05.007>
- 621 Crutchley, G.J., Geiger, S., Pecher, I.A., Gorman, A.R., Zhu, H., Henrys, S.A., 2010. The potential influence
622 of shallow gas and gas hydrates on sea floor erosion of Rock Garden, an uplifted ridge offshore of
623 New Zealand. *Geo-Marine Lett.* 30, 283–303. <https://doi.org/10.1007/s00367-010-0186-y>
- 624 Crutchley, G.J., Gorman, A.R., Fohrmann, M., 2007. Investigation of the role of gas hydrates in
625 continental slope stability west of Fiordland, New Zealand. *New Zeal. J. Geol. Geophys.* 50, 357–
626 364. <https://doi.org/10.1080/00288300709509842>
- 627 Deckers, J., 2015. Middle Miocene Mass Transport Deposits in the southern part of the Roer Valley
628 Graben. *Mar. Pet. Geol.* 66, 653–659. <https://doi.org/10.1016/j.marpetgeo.2015.07.006>
- 629 Dondurur, D., Küçük, H.M., Çifçi, G., 2013. Quaternary mass wasting on the western Black Sea margin,
630 offshore of Amasra. *Glob. Planet. Change* 103, 248–260.
631 <https://doi.org/10.1016/j.gloplacha.2012.05.009>
- 632 Ecker, C., Dvorkin, J., Nur, A.M., 2000. Estimating the amount of gas hydrate and free gas from marine
633 seismic data. *Geophysics* 65, 565–573. <https://doi.org/10.1190/1.1444752>
- 634 Egorov, V.N., Artemov, Y.G., Gulin, S.B., Polikarpov, G., 2011. Methane seeps in the Black Sea: discovery
635 , quantification and environmental assessment. *J. Black Sea/Mediterranean Environ.* 17, 171–185.
- 636 Egorov, V.N., Polikarpov, G.G., Gulin, S.B., Artemov, Y.G., Stokozov, N.A., Kostova, S.K., 2003. Present-
637 day views on the environment-forming and ecological role of the Black Sea methane gas seeps.
638 *Mar. Ecol. J.* 2, 5–26.
- 639 Elger, J., Berndt, C., Rüpke, L., Krastel, S., Gross, F., Geissler, W.H., 2018. Submarine slope failures due
640 to pipe structure formation. *Nat. Commun.* 9, 715. <https://doi.org/10.1038/s41467-018-03176-1>
- 641 Feldman, H.R., Lericolais, G., Dennielou, B., 2017. Exercise 10.2 - High-Resolution Seismic Stratigraphy
642 of the Danube Fan in the Black Sea, in: *Sequence Stratigraphy of Siliciclastic Systems*, SEPM
643 *Concepts in Sedimentology and Paleontology #9*. SEPM (Society for Sedimentary Geology).
- 644 Flood, R.D., Manley, P.L., Kowsmann, R.O., Appi, C.J., Pirmez, C., 1991. Seismic Facies and Late
645 Quaternary Growth of Amazon Submarine Fan, in: Weimer, P., Link, M.H. (Eds.), *Seismic Facies and*
646 *Sedimentary Processes of Submarine Fans and Turbidite Systems*. Springer New York, New York,
647 NY, pp. 415–433. https://doi.org/10.1007/978-1-4684-8276-8_23
- 648 Fraser, D.R.A., Gorman, A.R., Pecher, I.A., Crutchley, G.J., Henrys, S.A., 2016. Gas hydrate accumulations
649 related to focused fluid flow in the Pegasus Basin, southern Hikurangi Margin, New Zealand. *Mar.*
650 *Pet. Geol.* 77, 399–408. <https://doi.org/10.1016/j.marpetgeo.2016.06.025>

- 651 Gay, A., Lopez, M., Berndt, C., Séranne, M., 2007. Geological controls on focused fluid flow associated
652 with seafloor seeps in the Lower Congo Basin. *Mar. Geol.* 244, 68–92.
653 <https://doi.org/10.1016/j.margeo.2007.06.003>
- 654 Gay, A., Lopez, M., Cochonat, P., Seranne, M., Levache, D., Sermondadaz, G., 2006. Isolated seafloor
655 pockmarks linked to BSRs, fluid chimneys, polygonal faults and stacked Oligocene-Miocene
656 turbiditic palaeochannels in the Lower Congo Basin. *Mar. Geol.* 226, 25–40. <https://doi.org/DOI>
657 [10.1016/j.margeo.2005.09.018](https://doi.org/10.1016/j.margeo.2005.09.018)
- 658 Gillet, H., Lericolais, G., Rehault, J.-P., Dinu, C., 2003. La stratigraphie oligo-miocène et la surface
659 d'érosion messinienne en mer Noire, stratigraphie sismique haute résolution. *Comptes Rendus*
660 *Geosci.* 335, 907–916. <https://doi.org/10.1016/j.crte.2003.08.008>
- 661 Golmshtok, A.Y., Zonenshain, L., Terekhov, A., Shainurov, R., 1992. Age, thermal evolution and history
662 of the Black Sea Basin based on heat flow and multichannel reflection data. *Tectonophysics* 210,
663 273–293. [https://doi.org/10.1016/0040-1951\(92\)90326-2](https://doi.org/10.1016/0040-1951(92)90326-2)
- 664 Gorman, A.R., Holbrook, W.S., Hornbach, M.J., Hackwith, K.L., Lizarralde, D., Pecher, I., 2002. Migration
665 of methane gas through the hydrate stability zone in a low-flux hydrate province. *Geology* 30, 327.
666 [https://doi.org/10.1130/0091-7613\(2002\)030<0327:MOMGTT>2.0.CO;2](https://doi.org/10.1130/0091-7613(2002)030<0327:MOMGTT>2.0.CO;2)
- 667 Greinert, J., Artemov, Y., Egorov, V., De Batist, M., McGinnis, D., 2006. 1300-m-high rising bubbles from
668 mud volcanoes at 2080m in the Black Sea: Hydroacoustic characteristics and temporal variability.
669 *Earth Planet. Sci. Lett.* 244, 1–15. <https://doi.org/10.1016/j.epsl.2006.02.011>
- 670 Handwerger, A.L., Rempel, A.W., Skarbek, R.M., 2017. Submarine landslides triggered by destabilization
671 of high-saturation hydrate anomalies. *Geochemistry, Geophys. Geosystems* 18, 2429–2445.
672 <https://doi.org/10.1002/2016GC006706>
- 673 Heeschen, K.U., Haeckel, M., Klauke, I., Ivanov, M.K., Bohrmann, G., 2011. Quantifying in-situ gas
674 hydrates at active seep sites in the eastern Black Sea using pressure coring technique.
675 *Biogeosciences* 8, 3555–3565. <https://doi.org/10.5194/bg-8-3555-2011>
- 676 Heggland, R., 2005. Using gas chimneys in seal integrity analysis: a discussion based on case histories.,
677 in: Boulton, P., Kaldi, J. (Eds.), *Evaluating Fault and Cap Rock Seals*. Vol. 2. AAPG, Hedberg Series, pp.
678 237–245.
- 679 Ho, S., Cartwright, J.A., Imbert, P., 2012. Vertical evolution of fluid venting structures in relation to gas
680 flux, in the Neogene-Quaternary of the Lower Congo Basin, Offshore Angola. *Mar. Geol.* 332–334,
681 40–55. <https://doi.org/10.1016/j.margeo.2012.08.011>
- 682 Hornbach, M.J., Holbrook, W.S., Gorman, A.R., Hackwith, K.L., Lizarralde, D., Pecher, I., 2003. Direct
683 seismic detection of methane hydrate on the Blake Ridge. *Geophysics* 68, 92–100.
684 <https://doi.org/10.1190/1.1543196>
- 685 Horozal, S., Bahk, J.-J., Urgeles, R., Kim, G.Y., Cukur, D., Kim, S.-P., Lee, G.H., Lee, S.H., Ryu, B.-J., Kim, J.-
686 H., 2017. Mapping gas hydrate and fluid flow indicators and modeling gas hydrate stability zone
687 (GHSZ) in the Ulleung Basin, East (Japan) Sea: Potential linkage between the occurrence of mass
688 failures and gas hydrate dissociation. *Mar. Pet. Geol.* 80, 171–191.
689 <https://doi.org/10.1016/j.marpetgeo.2016.12.001>
- 690 Judd, A., Hovland, M., 2007. *Seabed Fluid Flow: The Impact on Geology, Biology and the Marine*
691 *Environment*. Cambridge University Press, Cambridge, UK.
- 692 Karstens, J., Berndt, C., 2015. Seismic chimneys in the Southern Viking Graben – Implications for palaeo
693 fluid migration and overpressure evolution. *Earth Planet. Sci. Lett.* 412, 88–100.

- 694 <https://doi.org/10.1016/j.epsl.2014.12.017>
- 695 Ker, S., Riboulot, V., 2015. GHASS Cruise Report, Ifremer. Ifremer, Brest, France.
- 696 Kessler, J.D., Reeburgh, W.S., Southon, J., Seifert, R., Michaelis, W., Tyler, S.C., 2006. Basin-wide
697 estimates of the input of methane from seeps and clathrates to the Black Sea. *Earth Planet. Sci.*
698 *Lett.* 243, 366–375. <https://doi.org/10.1016/j.epsl.2006.01.006>
- 699 Khosharay, S., Varaminian, F., 2013. Modeling interfacial tension of (CH₄+N₂)+H₂O and (N₂+CO₂)+H₂O
700 systems using linear gradient theory. *Korean J. Chem. Eng.* 30, 724–732.
701 <https://doi.org/10.1007/s11814-012-0187-9>
- 702 Klaucke, I., Sahling, H., Weinrebe, W., Blinova, V., Bürk, D., Lursmanashvili, N., Bohrmann, G., 2006.
703 Acoustic investigation of cold seeps offshore Georgia, eastern Black Sea. *Mar. Geol.* 231, 51–67.
704 <https://doi.org/10.1016/j.margeo.2006.05.011>
- 705 Koch, S., Berndt, C., Bialas, J., Haeckel, M., Crutchley, G., Papenberg, C., Klaeschen, D., Greinert, J., 2015.
706 Gas-controlled seafloor doming. *Geology* 43, 571–574. <https://doi.org/10.1130/G36596.1>
- 707 Konerding, P., 2008. Quaternary tectonics and seismic stratigraphy of the western Black Sea shelf. PhD
708 Thesis. University of Hamburg.
- 709 Kossel, E., Bigalke, N., Piñero, E., Haeckel, M., 2013. The SUGAR Toolbox - A library of numerical
710 algorithms and data for modelling of gas hydrate systems and marine environments.
711 Bremerhaven, Germany. <https://doi.org/10.10013/epic.41749.d002>
- 712 Kutas, R.I., Paliy, S.I., Rusakov, O.M., 2004. Deep faults, heat flow and gas leakage in the northern Black
713 Sea. *Geo-Marine Lett.* 24, 163–168. <https://doi.org/10.1007/s00367-004-0172-3>
- 714 Lericolais, G., Bourget, J., Popescu, I., Jermannaud, P., Mulder, T., Jorry, S., Panin, N., 2013. Late
715 Quaternary deep-sea sedimentation in the western Black Sea: New insights from recent coring and
716 seismic data in the deep basin. *Glob. Planet. Change* 103, 232–247.
717 <https://doi.org/10.1016/j.gloplacha.2012.05.002>
- 718 Li, A., Davies, R.J., Yang, J., 2016. Gas trapped below hydrate as a primer for submarine slope failures.
719 *Mar. Geol.* 380, 264–271. <https://doi.org/10.1016/j.margeo.2016.04.010>
- 720 Locat, J., Lee, H.J., 2002. Submarine landslides: advances and challenges. *Can. Geotech. J.* 39, 193–212.
721 <https://doi.org/10.1139/t01-089>
- 722 Løseth, H., Gading, M., Wensaas, L., 2009. Hydrocarbon leakage interpreted on seismic data. *Mar. Pet.*
723 *Geol.* 26, 1304–1319. <https://doi.org/10.1016/j.marpetgeo.2008.09.008>
- 724 Løseth, H., Wensaas, L., Arntsen, B., Hanken, N.M., Basire, C., Graue, K., 2011. 1000 m long gas blow-
725 out pipes. *Mar. Pet. Geol.* 28, 1040–1060. <https://doi.org/10.1016/j.marpetgeo.2010.10.001>
- 726 Lüdmann, T., Wong, H.K., Konerding, P., Zillmer, M., Petersen, J., Flüh, E., 2004. Heat flow and quantity
727 of methane deduced from a gas hydrate field in the vicinity of the Dnieper Canyon, northwestern
728 Black Sea. *Geo-Marine Lett.* 24, 182–193. <https://doi.org/10.1007/s00367-004-0169-y>
- 729 Maestrelli, D., Iacopini, D., Jihad, A.A., Bond, C.E., Bonini, M., 2017. Seismic and structural
730 characterization of fluid escape pipes using 3D and partial stack seismic from the Loyal Field
731 (Scotland, UK): A multiphase and repeated intrusive mechanism. *Mar. Pet. Geol.* 88, 489–510.
732 <https://doi.org/10.1016/j.marpetgeo.2017.08.016>
- 733 Manley, P.L., Pirmez, C., Busch, W., Cramp, A., 1997. Grain-size characterization of Amazon Fan deposits
734 and comparison to seismic facies units, in: Flood, R.D., Piper, D.J.W., Klaus, A., Peterson, L.C. (Eds.),

- 735 Proceedings of the Ocean Drilling Program Scientific Results. Ocean Drilling Program.
- 736 Martin, R.E., Yanko-Hombach, V., 2011. Rapid Holocene sea-level and climate change in the Black Sea:
737 An evaluation of the Balabanov sea-level curve, in: Geological Society of America Special Papers.
738 Geological Society of America, pp. 51–58. [https://doi.org/10.1130/2011.2473\(04\)](https://doi.org/10.1130/2011.2473(04))
- 739 Max, M.D., Johnson, A.H., 2014. Hydrate petroleum system approach to natural gas hydrate exploration.
740 *Pet. Geosci.* 20, 187–199. <https://doi.org/10.1144/petgeo2012-049>
- 741 Mazzini, A., Ivanov, M.K., Parnell, J., Stadnitskaia, A., Cronin, B.T., Poludetkina, E., Mazurenko, L., Van
742 Weering, T.C.E., 2004. Methane-related authigenic carbonates from the Black Sea: Geochemical
743 characterisation and relation to seeping fluids. *Mar. Geol.* 212, 153–181.
744 <https://doi.org/10.1016/j.margeo.2004.08.001>
- 745 McIver, R.D., 1982. Role of naturally occurring gas hydrates in sediment transport. *Am. Assoc. Pet. Geol.*
746 *Bull.* Vol. 66, 789–792.
- 747 Menard, H.W., 1955. Deep-sea channels, topography, and sedimentation. *Am. Assoc. Pet. Geol. Bull.* 39,
748 236–255.
- 749 Moscardelli, L., Wood, L., Mann, P., 2006. Mass-transport complexes and associated processes in the
750 offshore area of Trinidad and Venezuela. *Am. Assoc. Pet. Geol. Bull.* 90, 1059–1088.
751 <https://doi.org/10.1306/02210605052>
- 752 Moss, J.L., Cartwright, J., 2010. The spatial and temporal distribution of pipe formation, offshore
753 Namibia. *Mar. Pet. Geol.* 27, 1216–1234. <https://doi.org/10.1016/j.marpetgeo.2009.12.013>
- 754 Mountjoy, J.J., Barnes, P.M., Pettinga, J.R., 2009. Morphostructure and evolution of submarine canyons
755 across an active margin: Cook Strait sector of the Hikurangi Margin, New Zealand. *Mar. Geol.* 260,
756 45–68. <https://doi.org/10.1016/j.margeo.2009.01.006>
- 757 Mountjoy, J.J., Pecher, I.A., Henrys, S.A., Crutchley, G.J., Barnes, P.M., Plaza-Faverola, A., 2014. Shallow
758 methane hydrate system controls ongoing, downslope sediment transport in a low-velocity active
759 submarine landslide complex, Hikurangi Margin, New Zealand. *Geochemistry Geophys.*
760 *Geosystems* 15, 4137–4156. <https://doi.org/10.1002/2014GC005379>
- 761 Mulder, T., Alexander, J., 2001. The physical character of subaqueous sedimentary density flows and
762 their deposits. *Sedimentology* 48, 269–299. <https://doi.org/10.1046/j.1365-3091.2001.00360.x>
- 763 Mulder, T., Cochonat, P., 1996. Classification of Offshore Mass Movements. *SEPM J. Sediment. Res.* Vol.
764 66, 43–57. <https://doi.org/10.1306/D42682AC-2B26-11D7-8648000102C1865D>
- 765 Naudts, L., Greinert, J., Artemov, Y., Staelens, P., Poort, J., Van Rensbergen, P., De Batist, M., 2006.
766 Geological and morphological setting of 2778 methane seeps in the Dnepr paleo-delta,
767 northwestern Black Sea. *Mar. Geol.* 227, 177–199. <https://doi.org/10.1016/j.margeo.2005.10.005>
- 768 Nicoll, G.D., 2016. Comment on “Seismic chimneys in the Southern Viking Graben – Implications for
769 palaeo fluid migration and overpressure evolution” by Karstens and Berndt. *Earth Planet. Sci. Lett.*
770 <https://doi.org/10.1016/j.epsl.2015.11.038>
- 771 Olaru-Florea, R., Ungureanu, C., Rainer, T.M., Turi, V., Raileanu, A., 2014. Understanding of the
772 Petroleum System(s) of the Western Black Sea: Insights from 3-D Basin Modeling. *AAPG Search*
773 *and Discovery.* AAPG Search Discov. 10686, 1–20.
- 774 Panin, N., Popescu, I., 2007. The northwestern Black Sea: Climatic and sea-level changes in the Late
775 Quaternary, in: *The Black Sea Flood Question: Changes in Coastline, Climate, and Human*
776 *Settlement.* Springer Netherlands, pp. 387–404. https://doi.org/10.1007/978-1-4020-5302-3_16

- 777 Pape, T., Blumenberg, M., Seifert, R., Bohrmann, G., Michaelis, W., 2008. Links Between Geological
778 Processes, Microbial Activities & Evolution of Life, Links between Geological Processes, Microbial
779 Activities & Evolution of Life, Modern Approaches in Solid Earth Sciences. Springer Netherlands,
780 Dordrecht. <https://doi.org/10.1007/978-1-4020-8306-8>
- 781 Peckmann, J., Reimer, A., Luth, U., Luth, C., Hansen, B., Heinicke, C., Hoefs, J., Reitner, J., 2001.
782 Methane-derived carbonates and authigenic pyrite from the northwestern Black Sea. *Mar. Geol.*
783 177, 129–150. [https://doi.org/10.1016/S0025-3227\(01\)00128-1](https://doi.org/10.1016/S0025-3227(01)00128-1)
- 784 Phrampus, B.J., Hornbach, M.J., 2012. Recent changes to the Gulf Stream causing widespread gas
785 hydrate destabilization. *Nature* 490, 527–530. <https://doi.org/10.1038/nature11528>
- 786 Piper, D.J.W., Pirmez, C., Manley, P.L., Long, D., Flood, R.D., Normark, W.R., Showers, W., 1997. Mass-
787 transport deposits of the Amazon Fan, in: Flood, R.D., Piper, D.J., Klaus, A., Peterson, L.C. (Eds.),
788 Proceedings of the Ocean Drilling Program, 155 Scientific Results. Ocean Drilling Program, College
789 Station, TX, USA, pp. 109–146. <https://doi.org/10.2973/odp.proc.sr.155.212.1997>
- 790 Popescu, I., De Batist, M., Lericolais, G., Nouzé, H., Poort, J., Panin, N., Versteeg, W., Gillet, H., 2006.
791 Multiple bottom-simulating reflections in the Black Sea: Potential proxies of past climate
792 conditions. *Mar. Geol.* 227, 163–176. <https://doi.org/10.1016/j.margeo.2005.12.006>
- 793 Popescu, I., Lericolais, G., Panin, N., De Batist, M., Gillet, H., 2007. Seismic expression of gas and gas
794 hydrates across the western Black Sea. *Geo-Marine Lett.* 27, 173–183.
795 <https://doi.org/10.1007/s00367-007-0068-0>
- 796 Popescu, I., Lericolais, G., Panin, N., Normand, A., Dinu, C., Le Drezen, E., 2004. The Danube submarine
797 canyon (Black Sea): morphology and sedimentary processes. *Mar. Geol.* 206, 249–265.
798 <https://doi.org/10.1016/j.margeo.2004.03.003>
- 799 Popescu, I., Lericolais, G., Panin, N., Wong, H., Droz, L., 2001. Late Quaternary channel avulsions on the
800 Danube deep-sea fan, Black Sea. *Mar. Geol.* 179, 25–37. [https://doi.org/10.1016/S0025-3227\(01\)00197-9](https://doi.org/10.1016/S0025-3227(01)00197-9)
- 802 Popescu, S.-M., 2006. Late Miocene and early Pliocene environments in the southwestern Black Sea
803 region from high-resolution palynology of DSDP Site 380A (Leg 42B). *Palaeogeogr. Palaeoclimatol.*
804 *Palaeoecol.* 238, 64–77. <https://doi.org/10.1016/j.palaeo.2006.03.018>
- 805 Reeburgh, W.S., Ward, B.B., Whalen, S.C., Sandbeck, K.A., Kilpatrick, K.A., Kerkhof, L.J., 1991. Black Sea
806 methane geochemistry. *Deep Sea Res. Part A. Oceanogr. Res. Pap.* 38, S1189–S1210.
807 [https://doi.org/10.1016/S0198-0149\(10\)80030-5](https://doi.org/10.1016/S0198-0149(10)80030-5)
- 808 Riboulot, V., Cattaneo, A., Scalabrin, C., Gaillot, A., Jouet, G., Ballas, G., Marsset, T., Garziglia, S., Ker, S.,
809 2017. Control of the geomorphology and gas hydrate extent on widespread gas emissions offshore
810 Romania. *Bull. la Société géologique Fr.* 188, 26. <https://doi.org/10.1051/bsgf/2017182>
- 811 Riboulot, V., Ker, S., Sultan, N., Thomas, Y., Marsset, B., Scalabrin, C., Ruffine, L., Boulart, C., Ion, G.,
812 2018. Freshwater lake to salt-water sea causing widespread hydrate dissociation in the Black Sea.
813 *Nat. Commun.* 9, 117. <https://doi.org/10.1038/s41467-017-02271-z>
- 814 Rollet, N., Logan, G.A., Ryan, G., Judd, A.G., Totterdell, J.M., Glenn, K., Jones, A.T., Kroh, F., Struckmeyer,
815 H.I.M., Kennard, J.M., Earl, K.L., 2009. Shallow gas and fluid migration in the northern Arafura Sea
816 (offshore Northern Australia). *Mar. Pet. Geol.* 26, 129–147.
817 <https://doi.org/10.1016/j.marpetgeo.2007.07.010>
- 818 Römer, M., Sahling, H., Pape, T., Bahr, A., Feseker, T., Wintersteller, P., Bohrmann, G., 2012. Geological
819 control and magnitude of methane ebullition from a high-flux seep area in the Black Sea—the

820 Kerch seep area. *Mar. Geol.* 319–322, 57–74. <https://doi.org/10.1016/j.margeo.2012.07.005>

821 Seebeck, H., Tenthorey, E., Consoli, C., Nicol, A., 2015. Polygonal faulting and seal integrity in the
822 Bonaparte Basin, Australia. *Mar. Pet. Geol.* 60, 120–135.
823 <https://doi.org/10.1016/j.marpetgeo.2014.10.012>

824 Sheriff, R.E., 2011. *Encyclopedic dictionary of applied geophysics*, 4th ed. Society of Exploration
825 Geophysics, Tulsa, USA.

826 Starostenko, V.I., Rusakov, O.M., Shnyukov, E.F., Kobolev, V.P., Kutas, R.I., 2010. Methane in the
827 northern Black Sea: characterization of its geomorphological and geological environments. *Geol.*
828 *Soc. London, Spec. Publ.* 340, 57–75. <https://doi.org/10.1144/SP340.5>

829 Suess, E., 2014. Marine cold seeps and their manifestations: geological control, biogeochemical criteria
830 and environmental conditions. *Int. J. Earth Sci.* 103, 1889–1916. [https://doi.org/10.1007/s00531-](https://doi.org/10.1007/s00531-014-1010-0)
831 [014-1010-0](https://doi.org/10.1007/s00531-014-1010-0)

832 Sun, Q., Alves, T., Xie, X., He, J., Li, W., Ni, X., 2017. Free gas accumulations in basal shear zones of mass-
833 transport deposits (Pearl River Mouth Basin, South China Sea): An important geohazard on
834 continental slope basins. *Mar. Pet. Geol.* 81, 17–32.
835 <https://doi.org/10.1016/j.marpetgeo.2016.12.029>

836 Thöle, H., Kuhlmann, G., Lutz, R., Gaedicke, C., 2016. Late Cenozoic submarine slope failures in the
837 southern North Sea – Evolution and controlling factors. *Mar. Pet. Geol.* 75, 272–290.
838 <https://doi.org/10.1016/j.marpetgeo.2016.04.028>

839 Vanneste, M., De Batist, M., Golmshtok, A., Kremlev, A., Versteeg, W., 2001. Multi-frequency seismic
840 study of gas hydrate-bearing sediments in Lake Baikal, Siberia. *Mar. Geol.* 172, 1–21.
841 [https://doi.org/10.1016/S0025-3227\(00\)00117-1](https://doi.org/10.1016/S0025-3227(00)00117-1)

842 Vasilev, A., Dimitrov, L., 2002. Spatial and quantitative evaluation of the Black Sea gas hydrates. *Russ.*
843 *Geol. Geophys.* 43, 672–684.

844 Winguth, C., 1998. Pleistozäne Meeresspiegelschwankungen und Sedimentation im nordwestlichen
845 Schwarzen Meer. PhD Thesis. University of Hamburg.

846 Winguth, C., Wong, H.K., Panin, N., Dinu, C., Georgescu, P., Ungureanu, G., Krugliakov, V. V., Podshuveit,
847 V., 2000. Upper Quaternary water level history and sedimentation in the northwestern Black Sea.
848 *Mar. Geol.* 167, 127–146. [https://doi.org/10.1016/S0025-3227\(00\)00024-4](https://doi.org/10.1016/S0025-3227(00)00024-4)

849 Winters, W.J., Waite, W.F., Mason, D.H., Gilbert, L.Y., Pecher, I.A., 2007. Methane gas hydrate effect on
850 sediment acoustic and strength properties. *J. Pet. Sci. Eng.* 56, 127–135.
851 <https://doi.org/10.1016/j.petrol.2006.02.003>

852 Wong, H.K., Panin, N., Dinu, C., Georgescu, P., Rahn, C., 1994. Morphology and post-Chaudian (Late
853 Pleistocene) evolution of the submarine Danube fan complex. *Terra Nov.* 6, 502–511.
854 <https://doi.org/10.1111/j.1365-3121.1994.tb00894.x>

855 Wong, H.K., Winguth, C., Panin, N., Dinu, C., Wollschlager, M., Georgescu, P., Ungureanu, G., Krugliakov,
856 V. V., Podshuveit, V., 1997. The Danube and Dniepr fans, morphostructure and evolution.
857 *GeoEcoMarina* 2, 77–102.

858 Yoneda, J., Jin, Y., Katagiri, J., Tenma, N., 2016. Strengthening mechanism of cemented hydrate-bearing
859 sand at microscales. *Geophys. Res. Lett.* 43, 7442–7450. <https://doi.org/10.1002/2016GL069951>

860 Yun, T.S., Francisca, F.M., Santamarina, J.C., Ruppel, C., 2005. Compressional and shear wave velocities
861 in uncemented sediment containing gas hydrate. *Geophys. Res. Lett.* 32, L10609.

862 <https://doi.org/10.1029/2005GL022607>

863 Zander, T., Choi, J.C., Vanneste, M., Berndt, C., Dannowski, A., Carlton, B., Bialas, J., 2017a. Potential
864 impacts of gas hydrate exploitation on slope stability in the Danube deep-sea fan, Black Sea. *Mar.*
865 *Pet. Geol.* <https://doi.org/10.1016/j.marpetgeo.2017.08.010>

866 Zander, T., Haeckel, M., Berndt, C., Chi, W.-C., Klauke, I., Bialas, J., Klaeschen, D., Koch, S., Atgin, O.,
867 2017b. On the origin of multiple BSRs in the Danube deep-sea fan, Black Sea. *Earth Planet. Sci.*
868 *Lett.* 462, 15–25. <https://doi.org/10.1016/j.epsl.2017.01.006>

869